Nature Reviews Materials 6, 48–68 (2021). https://doi.org/10.1038/s41578-020-00236-1

Check for updates

Metallurgy, mechanistic models and machine learning in metal printing

T. DebRoy[1]✉, T. Mukherjee[1], H. L. Wei[2], J. W. Elmer[3] and J. O. Milewski[4]

Abstract | Additive manufacturing enables the printing of metallic parts, such as customized implants for patients, durable single-crystal parts for use in harsh environments, and the printing of parts with site-specific chemical compositions and properties from 3D designs. However, the selection of alloys, printing processes and process variables results in an exceptional diversity of microstructures, properties and defects that affect the serviceability of the printed parts. Control of these attributes using the rich knowledge base of metallurgy remains a challenge because of the complexity of the printing process. Transforming 3D designs created in the virtual world into high-quality products in the physical world needs a new methodology not commonly used in traditional manufacturing. Rapidly developing powerful digital tools such as mechanistic models and machine learning, when combined with the knowledge base of metallurgy, have the potential to shape the future of metal printing. Starting from product design to process planning and process monitoring and control, these tools can help improve microstructure and properties, mitigate defects, automate part inspection and accelerate part qualification. Here, we examine advances in metal printing focusing on metallurgy, as well as the use of mechanistic models and machine learning and the role they play in the expansion of the additive manufacturing of metals.

The printing of metals is the fastest growing sector[1] of additive manufacturing (AM) because of its capability to manufacture parts that cannot be made by other processes, soon after their design, while minimizing the number of processing steps[1–4]. In the printing of metals, the 3D design of a part is combined with manufacturing software to produce a solid metallic part. Parts are made in a layer-by-layer manner and using various heat sources and feedstocks. Aerospace, healthcare, energy, automotive, marine and consumer product industries all use printed metallic parts[2]. Examples of such parts include patient-specific metal implants[5], turbine blades with internal cooling channels[6], manifolds for engines and turbines, and lattice structures and truss networks with optimized strength to weight ratios[7]. Many parts that previously required assembly can now be printed as a single unit[3]. AM is also capable of fabricating parts with site-specific chemical compositions and properties[8].

The major variants of metal printing[1–3], either directed energy deposition (DED) or powder bed fusion (PBF), differ by the type of feedstock (powder or wire) and the heat source, either laser (L), electron beam (EB), plasma arc (PA) or gas metal arc (GMA) (FIG. 1). With the aid of computers, the motion of these heat sources is guided by a digital definition of the part, which results in the melting of metals, in a layer-by-layer manner, to construct 3D objects[1]. A focused laser or electron beam then selectively scans the surface and melts the powder particles into the desired shape for each successive layer, until the 3D part is printed[3]. By using very small diameter beams and tiny metal particles, intricate parts with fine and closely spaced features are printed. In DED, a powder or wire is supplied from above the build, whereas in PBF thin layers of powder, often thinner than human hair, are added after each layer is fused. These metal printing processes also differ in their heat source power, scanning speed, deposition rate, build size and other important attributes[3] (TABLE 1). The data show that the scanning speed and power vary widely depending on the specific process used. These variations result in an extreme 10,000-fold difference of the cooling rates, as well as vast differences in temperature gradient and heat input, not encountered in conventional materials processing[9]. The cooling rate and heat input affect the microstructure and properties of components, and, hence, these parameters must be controlled more carefully than those for the conventional processes to obtain good quality and reliable parts.

In DED, the feedstock, in the form of powder or wire, is melted either by a laser, an electron beam or an arc heat source. Unlike PBF, most DED processes are not confined by a bed or box of prescribed dimensions, allowing large parts to be created[1,3,10]. Wire-based DED is closely

[1]Department of Materials Science and Engineering, The Pennsylvania State University, University Park, PA, USA.
[2]School of Mechanical Engineering, Nanjing University of Science and Technology, Nanjing, China.
[3]Materials Engineering Division, Lawrence Livermore National Laboratory, Livermore, CA, USA.
[4]APEX3D LLC, Santa Fe, NM, USA.
✉e-mail: debroy@psu.edu
https://doi.org/10.1038/s41578-020-00236-1

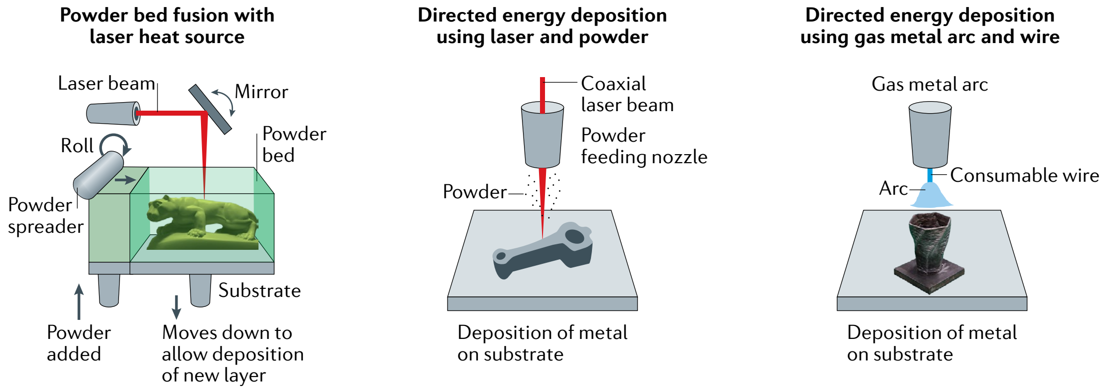

Fig. 1 | **Schematics of three metal printing processes.** Powder bed fusion with a laser heat source (left), directed energy deposition using a powder and laser heat source (middle) and directed energy deposition with a wire and gas metal arc heat source (right). Some important attributes[1–3,9,186,187,240] of these processes are shown in TABLE 1. Cup in right image is adapted from REF.[240], Springer Nature Limited.

related to conventional welding processes, and uses high powers to produce thick layers at high deposition rates to manufacture large parts economically[4]. Parts produced by DED-GMA, DED-PA and DED-L typically require machining owing to the high degree of surface waviness that results from large molten pools[1]. The exterior of a wavy part resembles the surface of a lake on a windy day with crests and troughs that scale with the AM layer height, which is smaller than the molten pool size. The electron beam processes are performed in a vacuum or in inert gas of low pressure allowing the processing of reactive metals, whereas the other heat sources require shielding of the parts using an inert gas[1]. Some AM processes do not require the melting of the feedstock. Instead, thin sheets and ribbons of metallic materials are consolidated by ultrasonic methods[1–3]. Alloy powders are also bound together by jetting a binder in a powder bed and then sintering in a high-temperature furnace[3].

AM processes have a large number of parameters, including the power and speed of the heat source, power density, feedstock geometry, delivery method and scanning pattern[9]. Parameter selection is important because it affects the shape and size of the molten pool, and the resulting thermal cycles, cooling rates, temperature gradients and solidification rates, which in turn determine the evolution of microstructure, defects and properties[1]. However, straightforward control of the microstructure, defects and properties remains elusive[2] because of the need to conduct many experiments to explore a large range of process parameters. The printing conditions are often selected based on the recommendations of the machine manufacturer or by trial and error[11]. Predictions of microstructures, properties and defects in printed parts require both theories of metallurgy and knowledge of how AM process parameters affect these features. However, metallurgical principles cannot predict the process variables needed to achieve good microstructures and mechanical properties. Mechanistic models and machine learning can provide the connection between process variables, part geometry, composition, microstructure, mechanical properties and defects for a given alloy. Such correlations are important because they can reduce the number of experiments needed to achieve high-quality parts.

Improving part quality by trial and error is not optimum for AM because of the high costs of feedstock and machines[9] combined with a changing economic culture where new products are rapidly created. Mechanistic models can predict physical attributes such as the temperature and velocity fields, microstructure and defect formation based on process variables, and thermophysical properties of alloys using phenomenological understanding[12]. If this understanding is lacking but data are available on process variables, alloy properties and product attributes, then machine learning[13] can make valuable contributions to the quality of printed parts. Starting from part design, process planning, process monitoring and control, machine learning can help reduce defects, achieve superior microstructures and properties, and facilitate product quality inspection for accelerated product qualification. The rapidly developing mechanistic models and machine learning algorithms can also open opportunities for printing new alloys[9]. The synergistic applications of metallurgy, mechanistic models and machine learning are important for the design, process planning, production, characterization and performance evaluation of printed parts (FIG. 2).

Metallurgy

Metallurgy has a mature knowledge base of processing, microstructure, properties and performance. Yet there are several issues of metal printing that cannot be understood using this knowledge. Printing of single crystals, parts with site-specific properties, superior combinations of properties not easily attainable by other manufacturing processes, unique metal matrix composites and parts with tailored solidification morphology and texture is complex and requires expansion of the existing knowledge base of metallurgy.

Printing single-crystal parts

AM layers are connected to the previous layer through melting, solidification and epitaxial growth, which creates metallurgical texture in the part. Texture may or may not be desirable but can be used advantageously in traditional directionally solidified or single-crystal parts where superior high-temperature creep resistance is required for aero-engine turbine parts[14]. AM is now being used in the fabrication and repair of single-crystal parts[15,16]. PBF and DED processes have made single-crystal, nickel-based superalloy parts using both laser and electron beam heat sources through control of solidification parameters[14–24]. For example, a CMSX-4 single-crystal cylinder 75 mm long and 12 mm in diameter was printed using PBF-EB[22] (FIG. 3a). The larger rupture strain of the heat-treated single crystal results in slightly longer creep life than conventionally processed alloys[14].

The most important requirement to print a single-crystal part is to maintain an appropriate combination of the temperature gradient and solidification growth rate to facilitate directional solidification[23]. These temperatures and growth rates can be achieved by preheating the powder bed[14,19–22] and using complex combinations of scanning pattern and speed[18,23]. More specifically, high power, a low scanning velocity and a moderate powder feeding rate were beneficial to fabricate single-crystal parts[23]. However, the directional solidification of single crystals still requires the optimization of some process conditions, including the preheat temperature, heat input and scanning strategy[25]. Well-tested mechanistic models of AM processes[26] can calculate the temperature gradients and the solidification growth rates based on which the conditions for directional solidification can be determined.

A common difficulty in printing single-crystal parts is the formation of stray grains. These grains[18,25] form primarily near the top edge of the deposit owing to high convective and radiative heat losses from the top surface of the molten pool that disrupts directional solidification. Stray grains are not observed in the interior layers because of their remelting. The regions with stray grains can be removed by machining. A quantitative understanding of printing single crystals is evolving. Developing high-fidelity mechanistic models of directional solidification in AM parts and databased machine learning need more work.

Site-specific properties

Parts such as gears and crankshafts require hard surfaces and soft cores, and AM enables the printing of such parts with site-specific properties. For a single-alloy part, site-specific properties can be achieved by tailoring the microstructure by controlling heat input and scanning strategies in both DED and PBF[8,27]. Varying grain size and tensile properties are achieved in an stainless steel 316 (SS 316) part printed using PBF-L by adjusting both the laser power and the scanning pattern[28].

In the functionally graded parts, site-specific properties can be achieved by varying the chemical composition and microstructure of parts over the desired distance. DED[29,30], PBF[31] and an AM process combining wire and powder[32] have been used to produce graded alloys. The compositional variation in a graded joint between ferritic 2.25Cr–1Mo steel and austenitic alloy 800H can be produced by DED-L (FIG. 3b). Such joints are useful for nuclear reactors but suffer from creep degradation at elevated temperatures because of the diffusive loss of carbon. The graded joint, when placed in service at 1,073 K, can significantly reduce carbon depletion by diffusion across the joint compared with joints between dissimilar alloys (FIG. 3b). As a result, a significant improvement in creep properties is achieved[30]. Also, a graded part between SS 304L and nickel alloy, Invar 36, was printed using DED-L to achieve a low coefficient of thermal expansion without sacrificing the strength and toughness of the part[33].

Table 1 | **Comparison of various parameters and attributes of three metal printing processes**

Parameter or process	Powder bed fusion with a laser or electron beam	Directed energy deposition using a powder and laser	Directed energy deposition using a wire (electron beam, plasma arc or gas metal arc)
Heat source power[3] (W)	50–1,000 (up to 4 beams)	400–3,000	1,000–5,000 (gas metal arc 2,000)
Scanning speed[1–3] (mm s^{-1})	10–1,000	6–60	5–50
Deposition rate[3,186] (cm^3 h^{-1})	25–180	20–450	100 to >1,000
Build size (mm × mm × mm)	Maximum 800 × 400 × 500	Maximum 2,000 × 1,500 × 1,000	Maximum 5,000 × 3,000 × 1,000
Feedstock diameter (μm)	15–60 (laser), 45–105 (electron beam)	15–105	900–3,000
Dimensional accuracy[186,187] (mm)	0.04–0.20	0.20–5	1–5
Surface roughness[1–3] (average deviation of surface from its mean height in μm)	7–30 (laser), 20–50 (electron beam)	15–60	45–200+, surface needs machining
Post processing	Heat treatment, hot isostatic pressing, machining	Heat treatment, machining, grinding	Heat treatment, stress relieving, machining
Cooling rate during solidification[1–3,9] (K s^{-1})	10^5–10^7	10^2–10^4	10^1–10^2
Temperature gradient[1–3,9] (K m^{-1})	10^6–10^7	10^5–10^6	10^3–10^4
Solidification growth rate[1–3,9] (m s^{-1})	10^{-1}–10^0	10^{-2}–10^{-1}	10^{-2}–10^{-1}

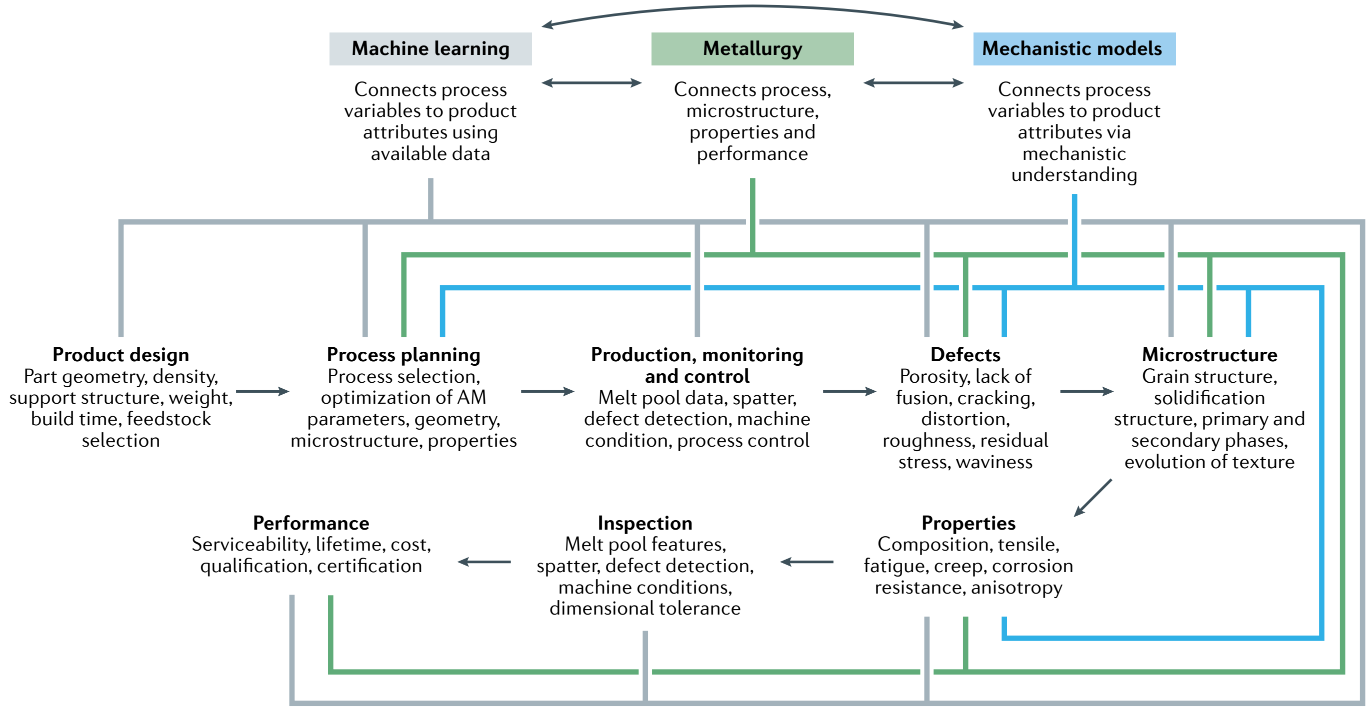

Fig. 2 | **Contributions of metallurgy, mechanistic models and machine learning in the various steps of metal printing.** The interrelation between machine learning, mechanistic models and metallurgy is shown by bidirectional black arrows. Some variables needed in machine learning, such as temperature, are difficult to measure but can be readily calculated using mechanistic models. The process–structure–properties–performance relations in metallurgy are complex and not always quantitative. Both mechanistic models and machine learning can provide a quantitative framework to understand metallurgical attributes of parts. The contributions of machine learning, metallurgy and mechanistic models in the various steps in the production and characterization of parts are shown by the grey, green and sky-blue lines, respectively. AM, additive manufacturing.

The AM of materials with site-specific properties is often challenging because of defects. For example, a graded part between Ti–6Al–4V to Invar 36 can fail[34] because of the formation of brittle intermetallic phases including FeTi, Fe_2Ti, Ni_3Ti and $NiTi_2$ in the gradient region. Unwanted phases are known to degrade the mechanical properties of parts[29,35]. Machine learning, combined with the metallurgical knowledge, has been used to find the optimum process parameters to avoid the formation of brittle phases[36].

Unique combination of properties

Combinations of superior properties of printed parts, not attainable by conventional manufacturing, have been reported. For example, the strength and ductility of stainless steel parts were simultaneously enhanced[37–41], defying the expected strength–ductility trade-off common in conventional manufacturing. This unusual behaviour has been attributed to hierarchal microstructure[37], dislocation networks that retard but do not prevent dislocation movements[37,38], nano-cellular structure in fine grains[39], unusual texture and twinning[40,41], and extremely fine solidification cells[41]. The presence of twinning in SS 316, built by PBF-L, has been suggested as a contributing factor for its ductility (FIG. 3c). In addition, the printed part shows increased strength and ductility, and a reduction of defects compared with a wrought alloy (FIG. 3c).

Improvements in strength without any degradation of ductility have also been reported in titanium alloys[42–48], SS 316L (REF.[49]) and 12CrNi2 (REF.[50]) and Al–12Si (REF.[51]) alloys. There are several different mechanisms for titanium alloys[42–48]. For example, rapid cooling during PBF-L of Ti–22Al–25Nb (REF.[43]) increases dislocation density owing to stress accumulation and forms a nanoscale hexagonal omega precipitate. Both a high dislocation density and precipitates hinder dislocation movement and contribute to the high strength without degradation of ductility. During solidification of Ti–6Al–4V, columnar grains of a body-centred cubic beta phase form. Subsequently, a hexagonal close-packed alpha phase grows inside the prior beta phase. The small sizes of both alpha and beta phases during DED-PA enhance strength[44]. In addition, heat treatment results in a globular shape of the alpha phase, enhancing toughness[46]. Rapid cooling of Ti–6Al–4V during PBF-L forms hexagonal close-packed martensite, which enhances strength[48]. Similarly, a fine-grain microstructure with nanoscale precipitates improves the mechanical properties of Ti185 alloy (Ti–Al–V–Fe)[47].

The aforementioned results are exciting, but the improvement in properties of alloys is not realized under all processing conditions[52]. This observation is hardly surprising because the cooling rate, temperature gradient and solidification growth rate vary considerably for different AM methods and processing conditions,

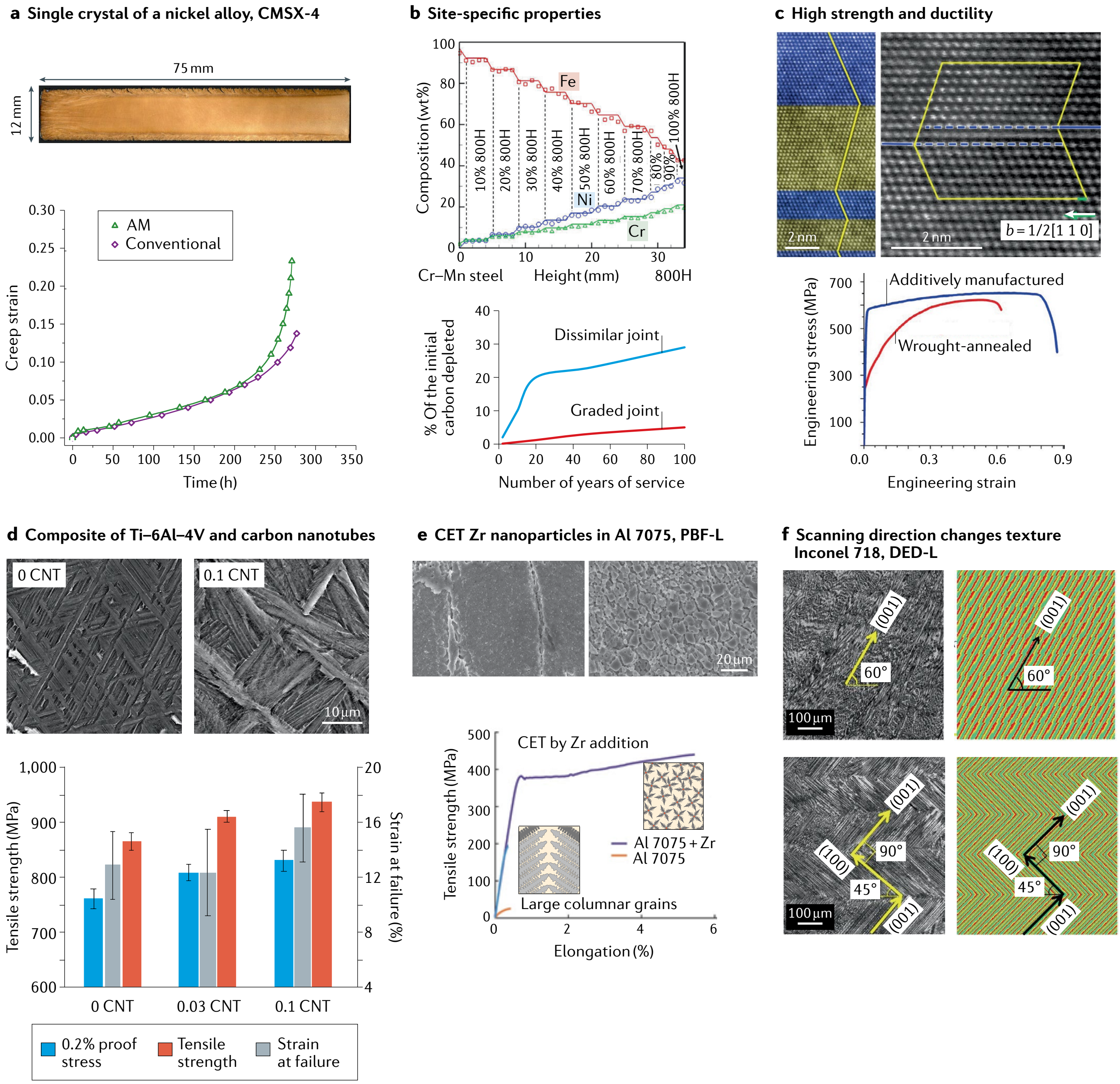

and, hence, the parts produced have a wide variety of microstructures and properties[9]. Further studies are required to understand the unusual microstructures and properties of printed metallic parts and their underlying mechanisms.

Composites

AM offers a means to synthesize unique metal matrix composites with excellent properties. Improvements in microstructure and properties have been observed by adding small amounts of non-metallic particles to the feedstock. This addition enables the incorporation of insoluble second-phase particles into the alloy, which contributes to mechanical loading or other property advantages, or creates second phases in situ to modify the base alloy by means of nucleation enhanced grain refinement. Examples include, Al, Ti and steel-based metal matrix composites of Al/Fe_2O_3, AlSi10Mg/SiC, Al/ZnO, Ti/C, Ti/SiC, Ti/Si_3N_4, Ti/Mo_2C and Fe/SiC[53].

Incorporation of second phases. TiC has been added to Inconel 718 (REFS[54,55]) and Inconel 625 (REF.[54]), and carbon nanotubes have been added to Inconel 625. Addition of nano-TiC to Inconel 718 strengthens the alloy[54,55] and reduces the coefficient of friction and wear rate[54]. These benefits have been attributed to a combination of three effects: changes in dislocation density owing to the residual plastic strain caused by the mismatch of thermal expansion between the two phases; the Orowan strengthening effect that represents strengthening owing to interaction between dislocations and small particles; and the Hall–Petch effect[54] that indicates higher strength

◀ Fig. 3 | **Properties of printed metallic components. a** | A single crystal[14] of a nickel alloy, CMSX-4, fabricated by powder bed fusion using an electron beam (top). The single crystal shows superior creep property compared with a conventionally manufactured part (bottom). **b** | Site-specific properties of a compositionally graded joint between a nickel alloy, 800H, and a chromium–manganese steel[30] fabricated by directed energy deposition using a laser beam (DED-L). Upper plot shows the variation of chemical composition along the build direction. Lower plot shows that the graded component significantly reduces the depletion of carbon compared with that from the dissimilar joint. **c** | Both improved strength and ductility can be achieved in a stainless steel part fabricated by DED-L[39]. Scanning tunnelling electron microscopy micrographs show atomic structures of the bunched nano-twins and twin boundary with a step. The twin and matrix are shown in blue and yellow, respectively (top). The magnitude and the direction of the lattice distortion (*b*: Burgers vector) is shown by the white arrow. The stress–strain plots of additively manufactured components show superior strength and ductility compared with the annealed wrought specimens (bottom). **d** | A composite material consisting of Ti–6Al–4V and carbon nanotubes (CNT) fabricated by directed energy deposition using a gas metal arc improves microstructure and mechanical properties[61] (top). Scanning electron microscopy images show reduction of the α lath length owing to the addition of carbon nanotubes. The addition of carbon nanotubes improves the 0.2% proof stress, tensile strength and strain at failure (bottom). **e** | A columnar to equiaxed transition (CET) and an improvement of toughness[66] occur on addition of zirconium nanoparticles to 7075 aluminium alloy (Al 7075) during powder bed fusion with a laser heat source (PBF-L). As a consequence of zirconium addition, the grain morphology changes from columnar (left) to equiaxed (right). The toughness improves because of the formation of equiaxed grains (bottom). **f** | Optical micrographs show changes in the direction of crystal growth depending on the scanning direction[82] for DED-L of Inconel 718. In the unidirectional scanning pattern, the growth direction of the primary dendrites was at an angle of about 60° with the horizontal scanning direction (top). If the laser beam is scanned in alternate directions in each layer, then the primary dendrites grow in a zig-zag pattern (bottom). Both modelling (right) and experimental (left) results are shown. AM, additive manufacturing. Panel **a** (top) adapted from REF.[22], CC BY 4.0. Panel **a** (bottom) adapted with permission from REF.[14], Elsevier. Panel **b** (top) adapted with permission from REF.[30], Elsevier. Panel **b** (bottom) constructed with data from REF.[30]. Panel **c** adapted with permission from REF.[39], Elsevier. Panel **d** adapted from REF.[61], Springer Nature Limited. Panel **e** adapted from REF.[66], Springer Nature Limited. Panel **f** adapted from REF.[82], Springer Nature Limited.

for smaller grain size. When added to Inconel 625, TiC changes texture[56] and significantly improves microhardness, tensile and wear properties. Small and optimal amounts of carbon nanotubes (0.25 wt%) increase both strength and ductility owing to grain boundary pinning and grain refinement[57].

Microstructural modification and grain refinement. Addition of TiB_2 particulates to AlSi10Mg results in textureless fine grains (average size 2 μm) and cells (<1 μm) with well-dispersed TiB_2 nanoparticles inside the grains and rod-like nano-Si precipitates inside the cells. Both the nano-Si and TiB_2 exhibited highly coherent interfaces because of sequential solidification[58]. Graphene oxide in an aluminium matrix noticeably improved the mechanical performance of the composite made by PBF-L as a result of Al_4C_3 nanorods formed in situ by the reaction of Al and graphene oxide[59]. Addition of carbon nanotubes to AlSi10Mg helped to achieve higher density[60] parts compared with parts without carbon nanotubes. TiB_2 in SS 316 reduced the size of the molten pool and disrupted the directional properties[49].

The addition of up to 0.1 wt% carbon in Ti–6Al–4V improved tensile strength and ductility because of the decrease in prior β grain size and α lath length[61]. The addition of carbon forms titanium carbide nanoparticles that act as grain refiners. FIGURE 3d indicates the microstructures of Ti–6Al–4V alloy with (left microstructure) and without (right microstructure) the addition of 0.1% carbon. The resulting strengthening effect owing to the refining of microstructures is also observed (FIG. 3d). The amount of additives is determined experimentally and more studies are needed to optimize the effects of carbon addition on the microstructure and properties of Ti–6Al–4V. A review of the fabrication, mechanical properties and defects in particle-reinforced nanocomposites made by selective laser melting indicates limited wettability of the nanoparticle and the tendency of the nanoparticles to agglomerate as important problems[62].

Columnar to equiaxed transition

The structure of printed alloys is often dominated by elongated columnar grains and strong texture[63–65] resulting in anisotropic properties, degradation of strength and the formation of cracks in many alloys[66,67]. Equiaxed grains with equal dimensions in all directions minimize crack formation and improve properties[58,66,67]. From our knowledge of welding and metal casting, there are two approaches to promote columnar to equiaxed transition (CET). The first approach relies on control of the processing conditions and alloy composition to generate favourable solidification conditions for equiaxed grain formation. These conditions consist of a low value for the temperature gradient to solidification rate ratio (G/R ratio) at the liquid/solid interface, which is the parameter that controls undercooling through the well-known constitutional supercooling mechanism[68]. The second approach relies on the introduction of small particles into the feedstock to create nuclei for equiaxed grain formation. These particles need to have low solubility in the molten pool and are often composed of elements with high melting points or non-metallic compounds.

Controlling the process parameters to promote a CET requires understanding that there is a maximum value of the G/R ratio for each alloy and there is no universal set of parameters favourable for equiaxed grain formation. In practice, adjustments of heat source power, scanning speed, hatch spacing, layer thickness and scanning strategy are useful to attain low G/R ratios that favour CET for each alloy. For example, CET was achieved during DED-L of Al–5Si–1Cu–Mg alloy by adjusting the layer thickness[69]. However, creating process conditions for producing low G/R ratios is challenging because the temperature gradient and solidification rate cannot be directly measured or independently controlled, and changes in process parameters can result in defects[70,71]. Solidification maps are available for many common alloys that can be helpful to achieve CET[72]. The chemical composition of the alloy can be further altered to restrain the growth of the columnar grains[68]. These methods rely on creating conditions that favour a wider range of G/R ratios for CET to occur through constitutional supercooling during regrowth from the previously deposited layers, rather than directly nucleating new grains ahead of the liquid/solid interface.

The second method for achieving CET is the addition of high melting point metallic or non-metallic nucleating agents with carefully selected crystallographic properties[58,66,68,73]. In this approach, intentionally designed low energy-barrier heterogeneous nucleating agents, often nano-particulate powders, are added to the feedstock material in small amounts, at quantities usually less than 1% (REF.[66]). It is also important to generate significant constitutional supercooling ahead of the solidifying dendrite tip to create conditions for nucleating agents to work, and the particles must be of appropriate size and chemistry to survive in the molten pool. These conditions require the composition, crystal structure, size and physical properties of a given nucleating agent to be considered in addition to its thermal surroundings in the molten pool in order to produce CET. For example, molybdenum, zirconium and La_2O_3 were added during DED-GMA of Ti–6Al–4V to form equiaxed grains[68]. CET was achieved in PBF-L of AlSi10Mg alloy by adding nano-TiB_2 (REF.[58]). A CET was observed by adding a small amount of zirconium nanoparticles to 7075 aluminium alloy and the strength and ductility were improved[66] (FIG. 3e). Control of solidification morphology by adjusting parameters that affect the temperature gradient and solidification rate as well as addition of a suitable inoculant has worked for several alloys and AM variants, but more work is needed to establish a database for controlling microstructures.

There are other approaches for promoting CET. For example, high-intensity ultrasound was used to achieve CET for both Ti–6Al–4V and Inconel 625 without requiring any changes in the process parameters or the addition of grain refiners[74]. Ultrasonic irradiation agitated the melt to produce a large number of nuclei in the alloy during solidification[74]. However, the application of this method requires modification of the printing equipment to enable generation of high-intensity ultrasound.

Texture

Texture, the non-random distribution of crystallographic orientations of a polycrystalline material, affects the properties of printed parts. These properties include the elastic modulus[75], yield and tensile strengths[76], ductility[76], fatigue resistance[77], corrosion behaviour[78,79], creep[80] and coefficient of thermal expansion. In metal printing, the regrowth of grains from previous layers is the source of columnar grains that grow epitaxially from the existing grains and tend to align with them[63]. This behaviour is modified by the size and shape of the molten pool, which tends to preferentially align the growing grains along the direction of local heat flow[81]. In PBF, columnar grains typically form along the growth direction[66], whereas in DED the direction of grain growth may deviate from the build direction[82]. The striking differences in the shape and size of the fusion zone in the two processes are contributing factors. However, in PBF and DED processes, texture is influenced by the competitive growth of grains depending on the direction of maximum heat flow as well as the preferred direction of crystal growth[26,63,72].

Texture creates anisotropic mechanical properties in the part, and it can be modified by post-build heat treatment[83]. During the building of parts, texture has been adjusted by varying the scanning speed, layer thickness, heat input, beam size and hatch spacing[84–86]. For example, texture of a cobalt-based alloy during laser deposition[87] was found to be affected by the scanning speed. The scanning strategy[81,88,89], processing variables and material systems[84] also affect texture. Experimental measurements of texture by electron backscatter diffraction[90], X-ray diffraction, ultrasonic evaluation[91,92] or neutron diffraction tend to be time consuming and expensive[93], so computational methods after rigorous validation are emerging to predict texture from the AM build parameters[94]. For example, the computed solidification patterns and the optical micrographs of the deposited Inconel 718 specimen for unidirectional and bidirectional scanning show the directions of grain growth (FIG. 3f). Striking differences[82] in the computed and the observed solidification textures owing to changes in laser scanning pattern during AM are also observed (FIG. 3f). The results show that modelling can predict and customize solidification textures.

Common defects

Defects such as voids and lack of fusion[95], cracking[66], residual stresses[96], distortion[96] and surface roughness all affect the properties and serviceability of parts. Voids can form owing to lack of fusion[95], keyhole instability[97,98] or gas-generated porosity[99]. If the laser or electron beam heat source is too intense, keyhole formation can occur with associated pores if the keyhole collapses due to instability[97]. If the heat source is not intense enough, the molten pool can be too shallow relative to the AM layer thickness or too narrow relative to the track spacing, resulting in a lack of fusion defects where insufficient molten metal is present to fuse the feedstock into the existing layer[95]. Porosity can occur whenever the feedstock or process conditions are such that oxygen, nitrogen, hydrogen or other gaseous elements are dissolved into the molten pool and, later, nucleate pores as the pool solidifies and gas solubility decreases[100]. The contaminant elements can come from external sources, such as improper inert gas shielding[100], or from gases within the powder or wire feedstock[101]. Post processing using hot isostatic pressing may be performed to minimize porosity and improve fatigue strength[1,102–104].

Cracks may form in AM parts during solidification and cooling to room temperature and are similar to the cracks that form during welding in crack-susceptible microstructures[66]. Solidification cracking is affected by the volumetric shrinkage of the molten pool depending on the alloy properties and liquid feeding in the inter-dendritic region during solidification. Solidification and liquation cracking occur in the fusion zone and the partially melted zone, respectively, when low melting-point phases create liquid films at grain boundaries that are pulled apart by tensile stresses during solidification[66]. The cracking sensitivity could be evaluated through a criterion[105] considering the separation of grains from each other, the lateral growth of grains and the ease of liquid feeding between grains.

Residual stresses develop from a liquid-to-solid change of state, thermal contraction and expansion, and from the use of fixtures, support structures and other forms of restraints[96,106]. In addition, solid-state phase transformations such as from austenite to ferrite in steels can contribute to residual stresses[106]. The stresses themselves can be large enough to cause delamination between AM layers in low-ductility alloys such as Ti–6Al–4V (REF.[107]), particularly if the part has other defects such as porosity or lack of fusion defects that may act as sites for stress concentration[108]. Residual stresses increase with the amount of restraint on the part being built[109] and tend to be lower for high heat inputs. As a consequence, heat treatment over long times allows the stresses to diminish. Distortion of AM parts depends on residual stresses, restraints, part stiffness and heat input[96]. Distortion can occur as the layer-by-layer part is created, causing the part to deviate from its intended geometry in a way that can be detrimental if precise dimensions are required[110].

Surface roughness and waviness are common in AM parts. Post-build processing, such as machining, grinding, chemical treatment or polishing, is often used to achieve a smooth surface[111,112]. The source of surface roughness depends on the sizes of the powder particles and processing conditions, and the surface waviness scales with the layer thickness[113,114]. Processes with high deposition rates, such as DED[115], make parts with more waviness than processes with low deposition rates, such as PBF[113]. However, the surfaces of the parts fabricated by PBF tend to be no smoother than the size of the largest powder particles, because unfused particles are observed near the solidified molten pools[116].

The scan strategy involves the remelting and sequential changes of the scan path direction coupled with the selection of the laser power and scan speed to optimize the reduction of porosity, lack of fusion, density, distortion and processing time. These difficulties have been shown to vary with the laser power, scan speed and hatch spacing. Porosity is frequently observed at the start or stop regions of a scan path or between the fusion zones of adjacent scan paths[100].

To conclude, it is difficult to control attributes of the printed parts by the selection of process parameters and feedstocks. These difficulties originate largely from the scarcity of quantitative frameworks that can correlate processing conditions with product attributes. Mechanistic models and machine learning address this difficulty by reducing the ranges of AM process variables to create parts with the desired attributes before parts are built while at the same time minimizing development times and costs.

Mechanistic models

Mechanistic models enable calculations of variables such as temperature and velocity fields, cooling rates and solidification parameters that are not easily measured during AM. These models provide a phenomenological description of how the microstructure and properties of an AM part evolve from process variables and the thermophysical properties of the feedstock. However, mathematical representation of the process and the product attributes is a challenging undertaking. This complexity is addressed, almost always, by modelling the most important physical processes and ignoring the less important processes. These assumptions compromise fidelity, the extent of which is checked by comparing model predictions with experimental results. In addition, the task is often leveraged using the experience of building models of fusion welding and metallurgy.

Mechanistic models of AM are widely used to predict the relationships between process variables and the attributes of parts. TABLE 2 summarizes some common mechanistic models, and their features and applications in metal printing. Many of the physical processes need to be represented in multiple length scales, and in some cases over varying timescales. Most of the simulations require transient 3D temperature fields. Considerable variation in the computational efficiency is achieved depending on the physical processes considered and the scale of calculations. When the calculations are performed on the mesoscale, they are fairly rapid. However, the same calculations in powder-scale models take orders of magnitude more time[117]. Therefore, linking of timescales and length scales is challenging and needs further research. Here, we examine the progress made and the opportunities and challenges in the mechanistic modelling of metal printing.

Models of heat transfer and metal flow

Metal printing involves heating, melting, solidification and solid-state phase transformations as well as the evolution of fusion zone geometry, microstructure, grain structure, defects, mechanical properties, residual stresses and distortion. A quantitative understanding of these physical processes and the attributes of the parts starts with simulation of the transient temperature field and the flow of liquid metal in the fusion zone. The heat transfer and fluid flow calculations are typically based on the equations of conservation of mass, momentum and energy to obtain important variables such as the temperature–time history, fusion zone geometry and solidification growth rates[118–120]. FIGURE 4a shows typical examples of the temperature and velocity fields of the molten pool during PBF-L, DED-L using powder and DED-GMA using wire feedstocks[120–122]. The 3D temperature distributions and geometries of the molten pool and the feedstock materials can be captured by the transport phenomena-based mesoscale models. These models can simulate deposition of parts in multiple layers, with each layer containing multiple tracks or hatches.

AM relies on the localized melting and solidification of feedstock materials and, as a result, the shape and size of the molten pool influence the microstructure and properties of the printed parts. Apart from calculating the geometrical features of the part, these models can calculate multiple thermal cycles experienced by the deposited metal during the build process. These results provide temperature–time data at various monitoring locations[118] (FIG. 4b). The thermal cycles are necessary for predicting microstructures. The experimental measurement of such exhaustive temperature–time–space data is challenging owing to the complex nature of AM. However, temperature–time data in several locations, when available, are useful to test and calibrate the models. The results obtained from the heat transfer and fluid flow models enable a quantitative understanding of the evolution of microstructure, grain structure and assessment of printability[123,124].

Table 2 | **Common mechanistic models for the simulation of metal printing**

Purpose	Model	Features	Applications
Calculation of heat, mass and momentum transfer	Part scale heat conduction model	Fourier heat conduction equation is solved either analytically in 1D or 2D or numerically in 3D Does not consider the effects of molten metal flow inside the pool and often provides inaccurate results	Temperature fields[188]; fusion zone geometry[189]; cooling rates[190]
	Part scale heat transfer and fluid flow	Solves 3D transient conservation equations of mass, momentum and energy Considers the effects of molten metal flow inside the pool and therefore provides accurate temperature distribution and deposit geometry	Temperature and velocity fields[119]; fusion zone geometry[121]; cooling rates[120]; solidification parameters[122]; lack of fusion[121]
	Part scale volume of fluid and level set methods	Tracks the free surface of the molten pool Computationally intensive Accumulates errors and the calculated deposit shape and size often do not agree well with experiments	3D deposit geometry[191]; temperature and velocity fields[191]; cooling rates[192]; solidification parameters[192]
	Powder-scale models	Involves free surface boundary conditions treating thermodynamics, surface tension, phase transitions and wetting Small timescale and length scale, computationally intensive Lattice Boltzmann or arbitrary Lagrangian Eulerian	Temperature and velocity fields[117]; track geometry[193]; lack of fusion[143]; spatter[143]; surface roughness[194]
Microstructure, nucleation and grain growth prediction	TTT-based[a], CCT-based[b] and JMA-based[c] models	Based on phase transformation kinetics during cooling Widely used for simulating phase transformations in steels and common alloys High computational efficiency	Solid-state phase transformation kinetics[195]
	Monte Carlo method	A probabilistic approach of grain orientation change Provides grain size distribution with time High computational efficiency	Grain growth[63]; solidification structure[26]; texture[40]
	Cellular automata	Simulates growth of grain and subgrain structure during solidification Medium accuracy and computational efficiency	Solidification structure[196]; grain growth[197]; texture[197]
	Phase field model	Simulates microstructural features and properties by calculating an order parameter based on free energy that represents the state of the entire microstructure Computationally intensive	Nucleation[132]; grain growth[198]; evolution of phases[198]; precipitate formation[199]; solid-state phase transformation[199]
Calculation of residual stresses and distortion	FEA-based[d] thermomechanical models	Solves 3D constitutive equations considering elastic, plastic and thermal behaviour Many software packages exist, and these are easy to implement and can handle intricate geometries Adaptive grid and inherent strain method are often used to increase calculation speed	Evolution of residual stress[200]; strains[138]; distortion[201]; delamination[165]; warping[165]

CCT, continuous cooling transformation; FEA, finite element analysis; JMA, Johnson–Mehl–Avrami; TTT, time–temperature–transformation. [a]TTT diagrams provide the effects of time and temperature on microstructure development of an alloy at constant temperature. [b]CCT diagrams indicate the phase changes during cooling. [c]The JMA equation provides the extent of phase transformations with time. [d]FEA is a numerical method to solve complex non-linear equations.

Simulation of microstructure evolution

Modelling of phase fractions of various constituents in the microstructure helps to understand the properties of printed parts both before and after their post-build heat treatment. Each heat-treatable alloy undergoes unique phase transformations during heating and cooling. As a result, modelling of microstructures is alloy-specific and represents the various pathways for each phase transformation involved in the evolution of microstructure[125]. There is a rich literature of microstructure calculations in multipass fusion welding where metallic materials are subjected to multiple thermal cycles, just like in AM processes[1]. In these systems and AM, reliable microstructure calculations have been achieved using detailed kinetic information[126] manifested in continuous cooling transformation diagrams and relations of phase fractions with time, such as the Johnson–Mehl–Avrami equation.

Simulations of phase transformations and the scale of microstructural features have been attempted considering the thermal history and alloy composition[127,128]. Microstructure calculations using the Johnson–Mehl–Avrami equation have been useful for PBF-L of the Ti–6Al–4V alloy[129], and continuous cooling transformation diagrams have been used[130] to understand microstructure evolution during DED-L of Ti–6Al–4V and for simulating precipitation kinetics during DED-L of Inconel 718 (REF.[131]). Although these calculations provide reliable results of phase fractions, they do not provide morphological information. Phase field simulations are used to resolve microstructural features in small length scales[132]. For example, phase field simulations

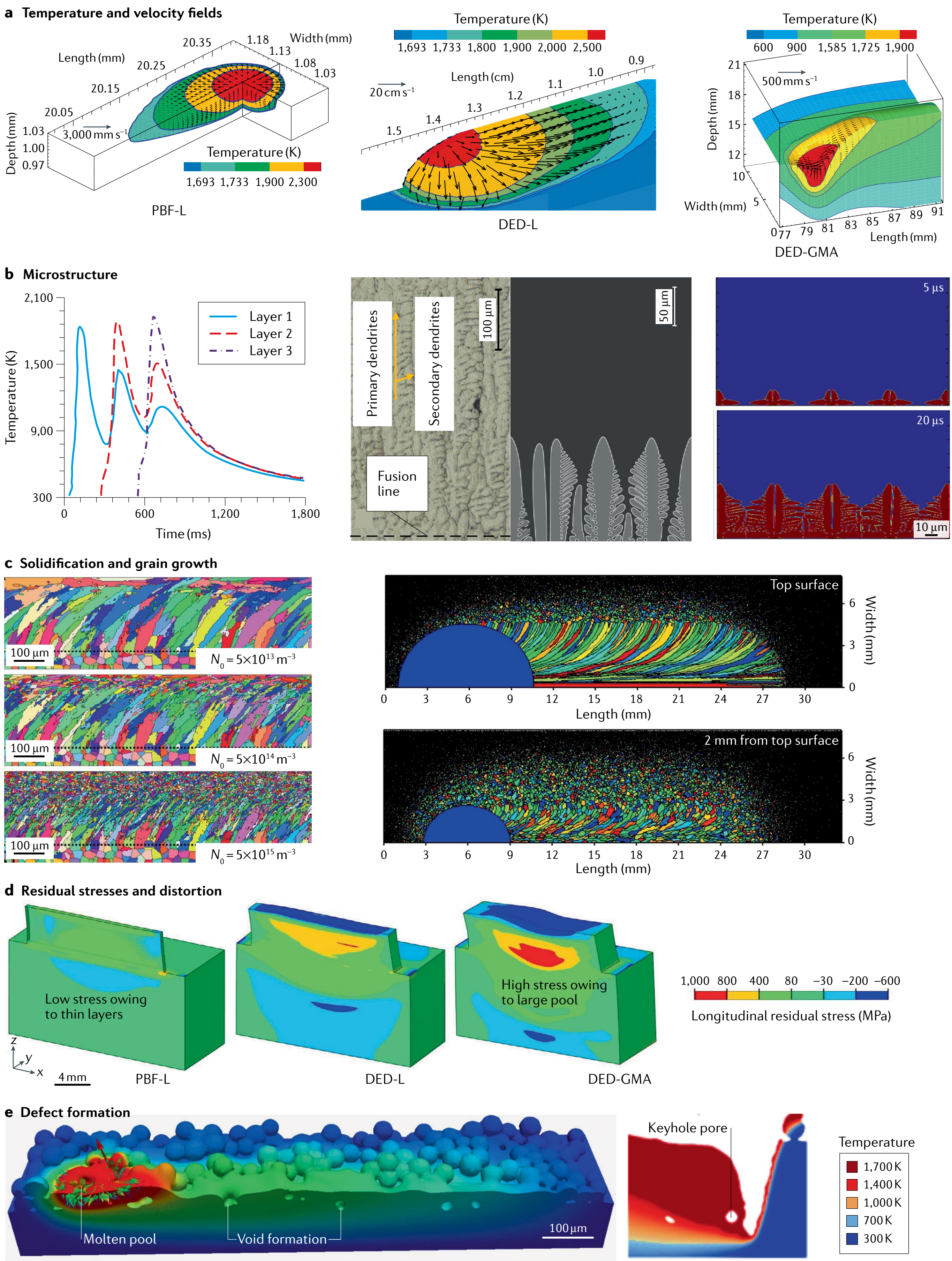
a Temperature and velocity fields
Length (mm)
20.35
20.25
20.15
20.05
1.18
1.13
1.08
1.03
Width (mm)
Depth (mm)
1.03
1.00
0.97
3,000 mm s−1
Temperature (K)
1,693 1,733 1,900 2,300
PBF-L
Temperature (K)
1,693 1,733 1,800 1,900 2,000 2,500
Length (cm)
20 cm s−1
1.5 1.4 1.3 1.2 1.1 1.0 0.9
DED-L
Temperature (K)
600 900 1,585 1,725 1,900
500 mm s−1
Depth (mm)
21 18 15 12 10
Width (mm) 5 0
77 79 81 83 85 87 89 91
Length (mm)
DED-GMA
b Microstructure
Temperature (K)
2,100
1,500
9,00
300
0 600 1,200 1,800
Time (ms)
Layer 1
Layer 2
Layer 3
Primary dendrites
Secondary dendrites
100 μm
Fusion line
50 μm
5 μs
20 μs
10 μm
c Solidification and grain growth
100 μm
N0 = 5×10^13 m−3
N0 = 5×10^14 m−3
N0 = 5×10^15 m−3
Top surface
2 mm from top surface
Width (mm)
6 3 0
0 3 6 9 12 15 18 21 24 27 30
Length (mm)
d Residual stresses and distortion
Low stress owing to thin layers
High stress owing to large pool
z y x
4 mm
PBF-L
DED-L
DED-GMA
1,000 800 400 80 −30 −200 −600
Longitudinal residual stress (MPa)
e Defect formation
Molten pool
Void formation
100 μm
Keyhole pore
Temperature
1,700 K
1,400 K
1,000 K
700 K
300 K

◀ Fig. 4 | **Results from various types of mechanistic models for metal printing.** **a** | Temperature and velocity fields in the molten pool of SS 316 stainless steel using continuum mechanics[120–122] for powder bed fusion with a laser (PBF-L), directed energy deposition with a laser (DED-L) and directed energy deposition with a gas metal arc (DED-GMA). The shape and size of the molten pool vary significantly for the different processes because of differences in process variables such as the power of the heat source and scanning speed. **b** | Plot of temperature as a function of time at a monitoring location showing multiple thermal cycles in different layers during DED-L of SS 316 (REF.[118]) (left). Phase field simulation of dendritic growth for gas tungsten arc welding of 2A14 aluminium alloy (REF.[133]) shows qualitative agreement between the experimentally observed microstructure on the left and the theoretically calculated microstructure on the right (middle). Phase field simulations of microstructure evolution electron beam additive manufacturing of Ti–6Al–4V (REF.[241]) showing temporal growth of beta phase columnar grains (right). **c** | The influence of nuclei density, N_0, on the morphologies of grains during PBF-L of SS 304 stainless steel shows that columnar to equiaxed transition is favoured at high nuclei density (left)[127]. Monte Carlo simulation of grain growth during gas tungsten arc welding of 1050A aluminium alloy shows that columnar grains may appear equiaxed at certain cross-sections because of the curvature of the columnar grains (right)[26]. **d** | Thermomechanical modelling of longitudinal residual stress and distortion in SS 316 parts made by PBF-L, DED-L and DED-GMA showing lower residual stress for PBF-L[123]. **e** | Powder-scale modelling of defect formation such as voids in PBF-L of Ti–6Al–4V. The shape and size of voids and their spatial distributions depend on the temperature field, molten pool geometry and powder size (left). Inappropriate selection of the power density of the laser beam causes porosity during keyhole-mode PBF-L of SS 316, which is simulated using a powder-scale model (right)[242]. Panel **a** (middle) adapted with permission from REF.[122], Elsevier. Panel **a** (right) adapted with permission from REF.[120], Elsevier. Panel **b** (left) adapted with permission from REF.[118], AIP. Panel **b** (middle) adapted with permission from REF.[133], Elsevier. Panel **b** (right) adapted from REF.[241], Springer Nature Limited. Panel **c** (left) adapted with permission from REF.[127], Elsevier. Panel **c** (right) adapted with permission from REF.[26], Elsevier. Panel **d** adapted from REF.[123] copyright © Institute of Materials, Minerals and Mining, adapted by permission of Informa UK Limited, trading as Taylor & Francis Group. Panel **e** (right) adapted from REF.[242], Springer Nature Limited.

of microstructure evolution[133] in an aluminium alloy show dendritic growth (FIG. 4b). Phase field simulations have also been applied for microstructure calculations in nickel-based superalloys[134]. Solid-state phase transformation from a beta phase to a basket-weave alpha phase that occurs during DED-L of Ti–6Al–4V (REF.[135]) has been investigated using a phase field model with temperatures computed from a powder-scale model. In these models, it is challenging to represent physical processes such as nucleation, heating and cooling considering fluid flow in 3D, and the specification of energy density fields especially at boundaries. Lack of quantitative comparisons of the evolution of phase fractions with experimental data and the computationally intensive nature of the 3D calculations at length scales comparable with the dimensions of the part add to the difficulties.

Calculation of grain structure evolution

The morphology, dimension and orientation of the grains affect the mechanical and chemical properties of parts. The spatial variations of grain size and morphology can be observed through serial sections along different directions. However, the procedure is time consuming. Also, depending on the plane selected, columnar grains may appear to be equiaxed grains in some sections. Models of grain growth based on Monte Carlo simulations or cellular automata have been used to understand the grain structure of printed parts. These models[26,63,136,137] can simulate the transition of different grain morphologies such as columnar to equiaxed grains, the variation of grain growth directions under location-dependent solidification conditions[26] and the solid-state grain growth under multiple thermal cycles[63]. The computed influence of nuclei density on the grain morphology shows that the quantities of equiaxed grains increase with the nuclei density and CET was observed where the nuclei density was large[127] (FIG. 4c, left).

The 3D grain growth model can uncover the evolution of grain structure and provide information about the morphology, dimension and orientation of the grains and texture[26,63,127]. These calculations require 3D transient temperature fields, fusion zone geometries, local temperature gradients and solidification growth rates at various locations, all of which can be obtained from heat and fluid flow modelling. Grains grow epitaxially from the partially melted grains and follow the maximum heat flow directions at the solidification front[26,63]. Modelling of grain structure in 3D is important because columnar grains may appear equiaxed in certain cross-sections[26,63] (FIG. 4c, right).

Modelling residual stress and distortion

Experimental determination of the evolution of stresses and distortion is challenging[1] but thermomechanical models[96,138] are widely used. These models are computationally intensive and are mostly based on heat conduction models that ignore liquid metal flow, which is typically the main mechanism for heat transfer within the molten pool. More accurate calculations that consider convective heat transfer are emerging with improvements in computational software and hardware. The distributions of residual stresses and strain along the laser scanning route vary significantly during PBF-L, DED-L and DED-GMA[123] (FIG. 4d). These calculations consider convective heat transfer and reveal that PBF-L shows minimum residual stresses and distortion because of the small size of the molten pool and the low deposition rate. Where computationally intensive calculations are not practical, back of the envelope analytical calculations[139] provide a means to mitigate distortion.

Models of defect formation

In mesoscale modelling, small-scale features such as surface roughness are not simulated. Powder-scale models are suitable for resolving these issues, because these models typically simulate 1 mm^3 or smaller volumes with a mesh size down to 1–2 μm[140]. The time step is often restricted to a few nanoseconds to maintain computation convergence at small grid spacing and high velocities of liquid metal flow[140]. Thus, these models can take a day or more, in multiprocessor computers, to simulate very small domains[141]. Void formation due to keyhole instability can be simulated by a powder-scale model (FIG. 4e).

Mechanistic models for the formation of various defects, such as porosity, loss of alloying elements and cracking, are emerging. Pores may form owing to lack of fusion during PBF and DED in commonly used AM alloys[121]. Keyhole induced pores were also simulated at high energy intensities capturing the unstable nature of keyhole walls[142,143]. Another important issue is the loss of alloying elements during the high temperature deposition. The selective loss of volatile alloying elements may result in a significant difference between the chemical composition of the feedstock and the deposit[123,124]. The change in composition also affects the microstructure and properties of the deposit.

The successful printing of many alloys is hindered by the cracking susceptibility[1] associated with the melting and solidification processes. Massive cracking often occurs at the boundaries of the columnar grains. Alternating the grain morphology from columnar to equiaxed can suppress the formation of solidification cracking and thus improve the printability of the alloy. Several approaches related to the metallurgy of CET are discussed above in 'Columnar to equiaxed transition'. All of these approaches need quantitative evaluations of the solidification conditions with appropriate transport phenomena and grain structure evolution models.

Estimation of printability

Printability is evaluated by examining susceptibilities of parts to common defects such as distortion, composition change, lack of fusion and cracking[123,124]. Comprehensive and reduced order models are available to undertake this task. A theoretical scaling analysis has been used to test the vulnerability of alloys to thermal distortion. Susceptibilities of alloys to lack of fusion defects has been calculated using numerical heat transfer and fluid flow calculations. A model-based printability database after experimental validation can reduce trial and error testing and expedite qualification of parts, and thus save time and money for the printing of new alloys.

At present, only a handful of commercial alloys can be easily printed, and the design of alloys specifically for AM is just beginning. An important goal is to improve the printability of alloys by making alloys less susceptible to common defects. For example, DED-L parts made from powders of Cr–Mo–V tool steel and a maraging steel exhibited superior mechanical properties to those from the individual steels[144]. Powder blends of titanium and chromium have been printed using DED-L to achieve good strength and ductility[145]. Silicon has been added to 2024, 6061 and 7075 aluminium alloys to reduce cracking arising from higher fluidity, decreased melting range, thermal expansion and solidification shrinkage[146]. Addition of rare earth elements such as scandium or zirconium to aluminium alloys resulted in fine precipitates of Al_3Zr or Al_3Sc that acted as inoculants for the grain refinement and prevention of cracking[146]. A new nickel-based Hastelloy was designed to prevent cracking during PBF-L[73].

Mechanistic models are powerful simulation tools that provide otherwise unobtainable insight[12]. However, these calculations require an understanding of underlying physical mechanisms that are not always available. In addition, mechanistic models are often complex and require significant computational resources and user skills. In contrast, machine learning requires less programming and modelling skills and, as a result, is being widely applied.

Machine learning in metal printing

Machine learning enables computers to make reliable predictions[147,148] by learning from data gathered from various sources. Useful information and relationships are extracted from data without phenomenological guidance or explicit programming. The accuracy of the predictions improves with the quality and volume of data. The availability of powerful open source programs facilitates their use for solving complex problems in metal printing that may appear intractable at first. Here, we examine the need for machine learning in metal printing, outline the availability of open source algorithms and codes, and discuss their effective use and impact in metal printing.

Reasons to use machine learning

Building high-quality parts by trial and error adjustment of multiple process variables is neither rapid nor cost-effective. As a result, machine learning[149–155] has been widely used in all steps of metal printing (FIG. 2). Evolution of the microstructure, properties and defects in metal printing depends on multiple simultaneously occurring physical processes. Therefore, unified, phenomenological predictions of the product attributes are not available. Machine learning can serve as a tool to predict the microstructure, properties and defects. It does not require the solution of complex equations based on phenomenological understanding and, as a result, the calculations are rapid[149]. In addition, the hierarchy of the input variables and their sensitivity on the output can be determined[155]. Finally, machine learning programs are easy to build owing to the availability of well-tested, easy to use and reliable algorithms.

Wide availability of resources

The application of machine learning in AM has been facilitated by machine learning models and open source programs (TABLE 3). Models for classification such as the decision tree, random forest and *k*-nearest neighbour are useful for data-classifying problems, such as the 'detected' or 'not-detected' pores in printed parts. These models are also used for decision-making. Regression-based models such as artificial neural networks, Bayesian networks and support vector machines are used to correlate the inputs and outputs based on a function and can predict the values of the output variables for a set of input parameters. Open source programs such as Weka, Scikit learning, TensorFlow, Keras and Theano can be easily used because they are accompanied by extensive manuals and test cases. In the next section, we examine the applications of machine learning in various phases of building metallic parts to improve product quality.

Applications in metal printing

The adoption of machine learning in metal printing has been driven by the need to manage process complexity and the availability of powerful open source codes. Recent applications range from process planning to parameter optimization, sensing and control, and result in improved fusion zone attributes, tailored microstructures and defect mitigation (FIG. 5). These examples

Table 3 | **Machine learning models, open source computer programs and their applications in metal printing**

Machine learning		Description and features	Applications in metal printing
Machine learning models	Artificial neural networks	Layers of hidden nodes connect input and output variables; an activation function is used to connect nodes with each other; errors in predictions are minimized by adjusting weights for each connection	Defect recognition[202]; geometry prediction[167]; thermal deformation compensation[203]; process parameter optimization[204]; anomaly detection[174]; quality monitoring[205,206]; topology optimization[207]
	Decision tree	Progressively classifies a group of variables based on rules and displays them as an upside-down tree; the root of the tree often displays the most important variable and the apex shows the least important variable	Surface roughness reduction[208]; porosity prediction[173]; dimensional variation[209]; printing speed modelling[210]; design considering residual stresses and support requirement[211]
	Support vector machines	Used for classification and regression, the model can split data into groups based on their locations in feature space; the features of the data fully determine their locations and there is no stochastic element involved	Defect detection[212]; real-time composition monitoring[213]; surface roughness[153]; tensile strength prediction[214]; construction of process maps[151]; monitoring temperature field[215]
	Bayesian networks or Bayesian classifiers	A statistical model that represents the probabilistic relation between cause and effect; the conditional probabilities are computed using Bayes' theorem	Quality inspection[216]; fault diagnosis[217]; thermal field prediction[218]; porosity prediction[219]; optimization of process parameters[220]; prediction of fusion zone depth[221]
	k-nearest neighbour	Separates data into different classes based on the attributes or the class of the majority of the nearest neighbours; the number of nearest neighbours, *k*, is selected by trial and error	Quality monitoring[154]; printing speed monitoring[210]; porosity prediction[173]; dimensional variation[209]; design of metamaterials[222]
	Random forest	Consists of multiple decision trees, each with a classification; the forest gets a classification from the attributes of the greatest number of trees; for regression, the model considers the average of the outputs of different trees	Surface roughness determination[208]; tensile strength prediction[214]; reducing macro porosity and cracks[223]; printing speed monitoring[210]; minimize porosity by optimizing parameters[158]
Open source computer programs	Weka	Written in Java; used for classification, clustering, regression and visualization; available from https://www.cs.waikato.ac.nz/ml/weka/citing.html (online course available)	Image classification-based defect detection[224]; energy consumption in additive manufacturing[225]; data classification[226]; fault diagnosis[217]; porosity reduction[227]
	Scikit learning	Written in Python, Cython, C and C++; used for classification, clustering and regression; available from https://scikit-learn.org/stable/	Printing speed modelling[210]; dimensional accuracy[228]; temperature profile prediction[229]; relation between several microstructures[230]; process monitoring[163]; grain structure simulation[231]
	TensorFlow	Written in Python, C++ and CUDA; used for neural network and data flow programming; available from https://www.tensorflow.org/	Dimensional accuracy[228]; defect detection[232]; mechanical behaviour of structures[233]; online monitoring of part quality[150]; molten pool images[234]
	Keras	Cross-platform neural network library written in Python; runs on multiple platforms; available from https://keras.io/	Distortion prediction[235]; thermal history prediction[236]; dimensional accuracy[228]; quality monitoring[237]
	Theano	Written in Python; Windows, Linux and Mac operating systems; available from http://www.deeplearning.net/software/theano	Defect detection[238]; prediction of part weight and building time[239]

illustrate the important role of machine learning in metal printing, either alone or in combination with mechanistic models.

Process parameter optimization. The selection of process parameters is the most important factor in controlling the quality of the part. Machine learning is a fast and reliable way to predict and optimize process conditions to achieve the desired attributes of a part (FIG. 5a). For example, neural networks for DED-GMA predicted the wire-feed rate, scanning speed, arc voltage and nozzle-to-plate distance to achieve the required width and height of the part[156,157]. A random forest algorithm was used to optimize process parameters to print good quality Inconel 718 parts using PBF-L[158]. Neural networks were used to predict translational and rotational speeds of the powder-spreading roller to minimize surface roughness[159]. A thermodynamic model was augmented with machine learning to identify process conditions to avoid the formation of a brittle intermetallic sigma phase during DED-L of a graded component between SS 316L and pure chromium[36]. Regression-based machine learning[160] was used to examine the influence of the feed rate, hatch spacing, laser power and powder feed rate of DED-L on the surface properties. The aforementioned applications of machine learning to build parts of several alloys using multiple AM variants indicate its ability to optimize process parameters based on data. The optimization of process parameters is improved as more data are accumulated with time.

Sensing and process control. Machine learning can be used to monitor and control metal printing, and, hence, to mitigate defect formation and improve dimensional accuracy. For example, in situ photographs of a part taken by a camera can be compared with the

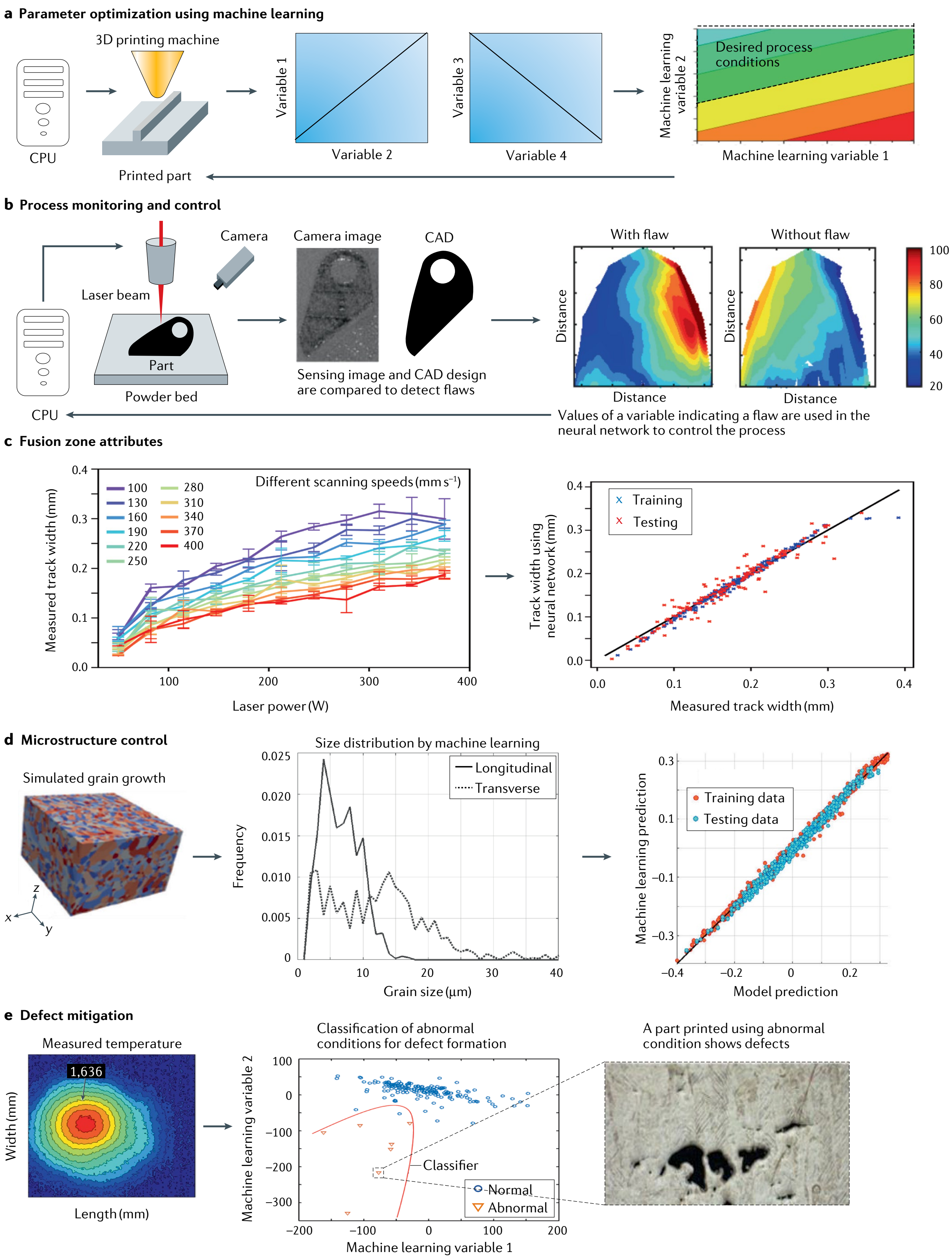
a Parameter optimization using machine learning
3D printing machine
CPU
Printed part
Variable 1
Variable 2
Variable 3
Variable 4
Machine learning variable 2
Desired process conditions
Machine learning variable 1
b Process monitoring and control
Camera
Camera image
CAD
Laser beam
Part
Powder bed
CPU
Sensing image and CAD design are compared to detect flaws
With flaw
Without flaw
Distance
Distance
Distance
Distance
100
80
60
40
20
Values of a variable indicating a flaw are used in the neural network to control the process
c Fusion zone attributes
Different scanning speeds (mm s⁻¹)
100
130
160
190
220
250
280
310
340
370
400
Measured track width (mm)
Laser power (W)
Training
Testing
Track width using neural network (mm)
Measured track width (mm)
d Microstructure control
Simulated grain growth
Size distribution by machine learning
Longitudinal
Transverse
Frequency
Grain size (µm)
Training data
Testing data
Machine learning prediction
Model prediction
e Defect mitigation
Measured temperature
1,636
Width (mm)
Length (mm)
Classification of abnormal conditions for defect formation
Machine learning variable 2
Classifier
Normal
Abnormal
Machine learning variable 1
A part printed using abnormal condition shows defects

◀ Fig. 5 | **Applications of machine learning in metal printing. a** | Schematic diagram showing the optimization of process parameters to obtain a desired attribute of a part, such as the deposit width, which depends on many process variables (variables 1–4). In machine learning, process variables are sometimes combined into fewer machine learning variables (machine learning variables 1 and 2) that can be obtained from the available data. These variables can be used to train a machine learning program to classify data (for example, greater than a specified width) or quantitatively correlate variables in the data with a target attribute (for example, deposit width). **b** | Optical images from each layer of a Ti–6Al–4V part is compared with the computer-aided design (CAD) file to identify regions of interest in the image that may include flaws during powder bed fusion using a laser heat source (PBF-L). These regions are split into subregions with spatial patterns in the image that are then fed into a neural network to identify flaws with good accuracy[161]. **c** | Track widths for different powers and speeds are measured using a high-speed camera and the data are used to train a neural network for the PBF-L of stainless steel 316 (left). The width predicted by the neural network agrees with the experimental data[166] (right). **d** | The grain growth results (left) from a computationally intensive Monte Carlo model provide grain size versus frequency data in two orthogonal directions (middle), longitudinal and transverse, that are used to train a neural network that could then rapidly calculate grain growth during directed energy deposition using a laser heat source (DED-L) (right)[171]. **e** | Temperature data near the fusion zone are measured by an infrared camera during DED-L of Ti–6Al–4V (left) and are correlated with the occurrence of porosity using a support vector machine (middle) that can predict porosity from the process variables[173]. CPU, central processing unit. Panel **a** (printing machine) adapted with permission from REF.[9], Elsevier. Panel **b** adapted with permission from REF.[161], ASME. Panel **c** adapted with permission from REF.[166], Wiley. Panel **d** adapted from REF.[171], Springer Nature Limited. Panel **e** adapted with permission from REF.[173], Elsevier.

computer-aided design to detect regions of interest that may contain flaws in a layer. These regions can be subdivided into several subregions with complex spatial patterns in the images that can be used to train a neural network to detect flaws in real time with good accuracy[161] (FIG. 5b). Three examples demonstrate various sensing and control methods. First, data on powder characteristics obtained using computer vision algorithms are used to train a support vector machine for process control[162]. Second, a process monitoring system augmented with a multilayer classifier[163] can provide control strategies for minimizing defect formation in PBF-L, based on data provided by identical machines producing the same part. Last, data from an optical sensor were analysed[164] using a support vector machine to detect defects during DED-L. These examples show the viability of in situ monitoring and control of the printing process with minimum human intervention.

Control of part geometry. Part geometry can deviate from the design specifications owing to instability in the printing process, and thermal distortion, and the deviation may result in part rejection in extreme cases[2,9,96,138,165]. Machine learning is often used to control part geometry during the printing process. For example, deposit widths measured using a high-speed camera during PBF-L of SS 316 for different laser powers and scanning speeds were used to train a neural network[166] (FIG. 5c, left). In another case, the neural network predicted the track width for a given scanning speed and laser power, which agreed well with the experimental results (FIG. 5c, right).

Neural network-based machine learning was used to control the deposit width and height, and the fusion zone depth, during DED-L of an aluminium alloy[167]. In addition, molten pool depth in PBF-L was controlled by optimizing laser power, scanning speed, spot size and absorptivity using a decision tree[168]. Furthermore, shape deviations were captured during the process and analysed using a neural network to achieve better geometric tolerance of AM parts[169]. These examples demonstrate the improved compliance with the geometric specifications of the design ultimately facilitating part qualification.

Tailoring microstructure and properties. Microstructural features such as grain size, distribution and orientation as well as properties such as tensile strength, hardness and fatigue life were used to develop machine learning algorithms that could rapidly compute processing conditions to achieve the desired microstructure and properties[170]. Input data for the training of machine learning can be generated from calibrated mechanistic models. For example, the results of frequency as a function of grain size computed using a 3D Monte Carlo model can be used to train a neural network (FIG. 5d). This neural network could rapidly predict grain growth, which matched well with the predictions from the computationally intensive Monte Carlo method[171] (FIG. 5d). A process model for PBF-EB supported by a neural network and a genetic algorithm predicted yield strength to aid in understanding the processing structure–property relationship for PBF process[172]. Although progress has been made in quantifying microstructural features using machine learning, the applications of machine learning to control microstructure and properties during metal printing remain in their initial stages of development.

Reducing defects. Machine learning has been used to minimize defects such as porosity, lack of fusion, distortion and surface roughness in parts. For example, machine learning has minimized the porosity in Ti–6Al–4V parts printed using DED-L[173] (FIG. 5e). More specifically, an infrared camera monitors the temperature field during the DED-L process, from which a molten pool boundary is extracted by tracking the solidus temperature contour. From the data, a support vector machine is developed that classifies the process conditions into two categories, normal and abnormal, based on the probability of porosity formation. When experiments were performed using the conditions for porosity formation, defects were found in the part (FIG. 5e). In another example, the anomalies in powder spreading by a recoater (a blade that spreads powder during PBF-L) were detected by a computer vision system[174]. Imperfections of the powder bed resulting from recoater streaking and hopping were correlated with part defects using a neural network. In other studies, automated image analysis has been used to detect anomalies during the powder spreading of PBF-L to identify defects using machine learning[175]. Machine learning provides an excellent framework for the reduction of surface defects, the origin of which are not always known.

Other applications. Apart from the various stages of building parts, machine learning has other uses in metal printing, including powder characterization, part failure and in situ part inspection. For example, a support vector machine trained using the data from computer vision was used to quantify powder characteristics[162]. Machine learning has been used to predict equipment failure and proactively anticipate and print replacement parts before the actual failure[176]. In essence, the machine learning platform is trained with high-resolution camera imaging and computed tomography scan data, and can eventually 'learn' to predict problems and detect defects in the printing process[177]. Computer vision technology and machine learning are already used in industry to perform an inspection of parts and identify microscopic cracks in the printed parts to save time and money[177].

Effective use and impact

The selection of algorithms and the quality and volume of data affect the accuracy, reliability and speed of the solutions[149]. For example, a data-classifying problem such as the 'detected' or 'not-detected' pores in printed metal parts is best addressed by an attribute-based classifier algorithm, such as random forest or decision tree, rather than a regression-based neural network[147]. The machine learning literature[147] guides the selection of algorithms for different classes of problems.

The common issues of data quality, features, imbalance and scarcity can be addressed using data improvements available in the literature[149]. Not all variables in metal printing influence the part attributes equally and the selection of input data is important[13]. Besides, the available data need to be checked for reproducibility and errors. The scarcity of data for the algorithms is a common problem[13] in AM and data augmentation techniques can artificially increase the volume of data[148]. However, duplication of a biased data set for a classification problem may lead to poor accuracy of a neural network owing to overfitting[147]. Some algorithms such as support vector machines[147] can be effective for small data sets.

The impact of machine learning may be further enhanced by the capabilities of other digital tools, such as mechanistic models. For example, the simultaneous application of a mechanistic model and machine learning in AM has been used in the related field of welding[178]. Peak temperatures, cooling rates, solidification parameters and other results obtained from validated mechanistic models can serve as a source of valuable data for machine learning. In dealing with the scarcity of data, mechanistic models can provide certain features of data or, in some cases, add to the volume of data to increase efficiency and reliability of machine learning. Such hybrid models may have new capabilities beyond improving speed and accuracy.

Research needs

The printing of metallic parts with advanced properties and functionality has attracted considerable interest in diverse industries. However, AM faces considerable scientific, technological and commercial challenges[2,179]. These challenges include the difficulties in controlling microstructure, properties and defects, as well as a lack of standards, a slow rate of printing, scarcity of feedstock materials for many commercial alloys and cost-competitiveness[2,11,179].

The scientific challenges originate, to a large extent, from the diverse heat input and cooling rates and the complex thermal cycles that affect the microstructure, properties and defects[1,2]. The microstructure–property–performance relationships of many alloys are currently being investigated. However, the high dislocation density, segregation of alloying elements, elongated grains and fine microstructural features are complicating factors for the control of microstructure and properties of printed parts. Better understanding of the mechanisms for the simultaneous improvements of multiple properties such as strength and ductility[37–41] would enrich scientific understanding of AM and metallurgy. A unified approach for the control of solidification morphology and texture based on mechanistic models and machine learning would accelerate our understanding of texture[2]. Improved theoretical and experimental control of morphology would also benefit the repair of single-crystal turbine blades[17]. Advanced computational frameworks for the control of defects such as lack of fusion, residual stresses and distortion will help to reduce defects in parts to the levels seen in wrought metal[2,180].

Standards are being developed to assist in materials and part qualification. Currently, parts are qualified by trial and error building and testing of parts[2]. Predictions of solidification structure, grain growth and solid-state phase transformations using mechanistic models before printing will be useful to select the parameter space for testing and greatly reduce the time and effort needed for qualification. Similarly, developing high-fidelity mechanistic models can be helpful for minimizing distortions and residual stresses prior to building. Models of lack of fusion defects are currently being developed to avoid conditions for their formation. Multiscale models balancing the spatial and temporal resolutions and computational efficiencies are needed[12].

Machine learning enables the improvement of the quality of printed parts by supporting almost every step of metal printing, ranging from product design to process planning to process monitoring and control[150–154] (FIG. 2). The research needs for machine learning include the classification and analysis of quality data sets to generate training, validation and testing sets and the identification of appropriate algorithms[181]. The large data set generated for different combinations of AM variants, process parameters and alloys is difficult to analyse, interpret and classify to train and test the machine learning algorithms[181,182]. Advanced digital tools and algorithms are needed for data analysis and successful implementation of machine learning in AM.

The implementation of mechanistic models and machine learning in conventional processing is often undertaken[183] using a digital twin. A digital twin of AM can build and test a virtual part prior to building the physical one, thus making decisions based on scientific principles and data for achieving high-quality parts. The utility of digital twins is well established[183] but they are not yet generally available for AM. Significant research and development are required[9,122] to construct or modify the building blocks of a digital twin and test them for various combinations of alloys and AM processes.

Outlook

The recent growth in sales of commercial AM equipment, the number of patents granted globally and the market revenue all point to the expansion of AM in the foreseeable future[1,2,11,179]. The growth of AM in niche applications aided by large corporations will undoubtedly continue because of the advantages of metal printing over conventional processing. However, the value of all 3D printed products is now only about US$7.3 billion, which is insignificant in comparison with the estimated value of US$13 trillion for the global manufacturing industry[184]. Significant expansion of AM — more specifically, the printing of many more commercial alloys by enterprises of all sizes — will depend on our ability to overcome the bottlenecks within AM[2].

The recent literature on AM points to three unmistakable trends. First, the method adapted to solve many of the problems faced by AM will not follow the path by which technologies matured in the past[2]. The growing applications of mechanistic models and machine learning to select process parameters will improve part quality, lower cost and reduce the volume of trial and error experiments for qualifying parts. Second, the layer-by-layer printing of metals, sometimes with layers thinner than a human hair, is uncovering puzzling scientific issues related to microstructure and properties[2]. Multidisciplinary research to solve these problems is already advancing the practice of AM and contributing to the science of metallurgy[2]. Last, 3D printing is improving conventional manufacturing. 3D printed injection moulds with intricate internal cooling channels are reducing cooling times and improving productivity and part quality; printed milling machine tools and heads are extending tool life; 3D printing is enabling low-cost repair of machine tools; and parts are additively made and machined in one operation by hybrid CNC (computer numerical control) machines with 3D printing capability. Thus, the contributions of metallurgy, mechanistic models and machine learning to metal printing are permeating into conventional manufacturing.

In the future, it is likely that metal printing hardware will include appropriate electronics to embody and use the printability database[123,124] to its advantage. Here, a printability database can be used to avoid problems such as solidification cracking of parts and other defects that are persistent problems in AM. For example, a smart AM machine can perform preheating of a powder bed to avoid part cracking[1] in some alloys under certain AM conditions. The machine may also progressively update process–microstructure–property relations with experience. Selected mechanistic models can provide guidance to select AM parameters to minimize porosity resulting from keyhole instability[1] and to reduce lack of fusion defects[185] owing to insufficient overlap of adjacent scan paths. Integrating machine learning algorithms with the hardware will help to control part geometry and make in situ adjustment of process variables to correct part shape and reduce defects. Such systems will collect and use data, control the building process and routinely produce reliable parts at low cost with minimal human intervention. The scientific, technological and economic challenges faced by metal printing[2] will be addressed by advances in software and hardware to facilitate mechanistic models and machine learning, and will continuously improve printability database and microstructure–property correlations. These advancements will require worldwide availability of a multidisciplined and technologically orientated workforce to integrate these separate fields of expertise into new metal printing systems[2,9,11].

Published online: 02 October 2020

1. DebRoy, T. et al. Additive manufacturing of metallic components — process, structure and properties. *Prog. Mater. Sci.* **92**, 112–224 (2018).
2. DebRoy, T. et al. Scientific, technological and economic issues in metal printing and their solutions. *Nat. Mater.* **18**, 1026–1032 (2019).
3. Milewski, J. O. *Additive Manufacturing of Metals: From Fundamental Technology to Rocket Nozzles, Medical Implants, and Custom Jewelry* Vol. 258 (Springer, 2017).
4. Sames, W. J., List, F. A., Pannala, S., Dehoff, R. R. & Babu, S. S. The metallurgy and processing science of metal additive manufacturing. *Int. Mater. Rev.* **61**, 315–360 (2016).
5. Bose, S., Ke, D., Sahasrabudhe, H. & Bandyopadhyay, A. Additive manufacturing of biomaterials. *Prog. Mater. Sci.* **93**, 45–111 (2018).
6. Shinde, M. S. & Ashtankar, K. M. Additive manufacturing — assisted conformal cooling channels in mold manufacturing processes. *Adv. Mech. Eng.* **9**, 1687814017699764 (2017).
7. Qi, D. et al. Mechanical behaviors of SLM additive manufactured octet-truss and truncated-octahedron lattice structures with uniform and taper beams. *Int. J. Mech. Sci.* **163**, 105091 (2019).
8. Tammas-Williams, S. & Todd, I. Design for additive manufacturing with site-specific properties in metals and alloys. *Scr. Mater.* **135**, 105–110 (2017).
9. Mukherjee, T. & DebRoy, T. A digital twin for rapid qualification of 3D printed metallic components. *Appl. Mater. Today* **14**, 59–65 (2019).
10. Elmer, J. et al. Wire-based additive manufacturing of stainless steel components. *Weld. J.* **99**, S8–S24 (2020).
11. Gao, W. et al. The status, challenges, and future of additive manufacturing in engineering. *Comput. Aid. Des.* **69**, 65–89 (2015).
12. Francois, M. M. et al. Modeling of additive manufacturing processes for metals: challenges and opportunities. *Curr. Opin. Solid State Mater. Sci.* **21**, 198–206 (2017).
13. Qi, X., Chen, G., Li, Y., Cheng, X. & Li, C. Applying neural-network-based machine learning to additive manufacturing: current applications, challenges, and future perspectives. *Engineering* **5**, 721–729 (2019).
14. Bürger, D., Parsa, A., Ramsperger, M., Körner, C. & Eggeler, G. Creep properties of single crystal Ni-base superalloys (SX): a comparison between conventionally cast and additive manufactured CMSX-4 materials. *Mater. Sci. Eng. A* **762**, 138098 (2019).
15. Acharya, R., Bansal, R., Gambone, J. J. & Das, S. A coupled thermal, fluid flow, and solidification model for the processing of single-crystal alloy CMSX-4 through scanning laser epitaxy for turbine engine hot-section component repair (Part I). *Metall. Mater. Trans. B* **45**, 2247–2261 (2014).
16. Acharya, R., Bansal, R., Gambone, J. J. & Das, S. A microstructure evolution model for the processing of single-crystal alloy CMSX-4 through scanning laser epitaxy for turbine engine hot-section component repair (Part II). *Metall. Mater. Trans. B* **45**, 2279–2290 (2014).
17. Basak, A., Acharya, R. & Das, S. Additive manufacturing of single-crystal superalloy CMSX-4 through scanning laser epitaxy: computational modeling, experimental process development, and process parameter optimization. *Metall. Mater. Trans. A* **47**, 3845–3859 (2016).
18. Liang, Y.-J., Cheng, X., Li, J. & Wang, H.-M. Microstructural control during laser additive manufacturing of single-crystal nickel-base superalloys: new processing–microstructure maps involving powder feeding. *Mater. Des.* **130**, 197–207 (2017).
19. Meid, C. et al. Effect of heat treatment on the high temperature fatigue life of single crystalline nickel base superalloy additively manufactured by means of selective electron beam melting. *Scr. Mater.* **168**, 124–128 (2019).
20. Pistor, J. & Körner, C. Formation of topologically closed packed phases within CMSX-4 single crystals produced by additive manufacturing. *Mater. Lett. X* **1**, 100003 (2019).
21. Ramsperger, M. et al. Solution heat treatment of the single crystal nickel-base superalloy CMSX-4 fabricated by selective electron beam melting. *Adv. Eng. Mater.* **17**, 1486–1493 (2015).
22. Körner, C. et al. Microstructure and mechanical properties of CMSX-4 single crystals prepared by additive manufacturing. *Metall. Mater. Trans. A* **49**, 3781–3792 (2018).
23. Liang, Y.-J. et al. Experimental optimization of laser additive manufacturing process of single-crystal nickel-base superalloys by a statistical experiment design method. *J. Alloy. Comp.* **697**, 174–181 (2017).
24. Butler, T. M., Brice, C. A., Tayon, W. A., Semiatin, S. L. & Pilchak, A. L. Evolution of texture from a single crystal Ti–6Al–4V substrate during electron beam directed energy deposition. *Metall. Mater. Trans. A* **48**, 4441–4446 (2017).
25. Zhou, Z. et al. Causes analysis on cracks in nickel-based single crystal superalloy fabricated by laser powder deposition additive manufacturing. *Mater. Des.* **160**, 1238–1249 (2018).

26. Wei, H. L., Elmer, J. W. & DebRoy, T. Three-dimensional modeling of grain structure evolution during welding of an aluminum alloy. *Acta Mater.* **126**, 413–425 (2017).
27. MacDonald, E. & Wicker, R. Multiprocess 3D printing for increasing component functionality. *Science* **353**, aaf2093 (2016).
28. Niendorf, T. et al. Functionally graded alloys obtained by additive manufacturing. *Adv. Eng. Mater.* **16**, 857–861 (2014).
29. Bobbio, L. D. et al. Analysis of formation and growth of the σ phase in additively manufactured functionally graded materials. *J. Alloy. Comp.* **814**, 151729 (2020).
30. Zuback, J., Palmer, T. & DebRoy, T. Additive manufacturing of functionally graded transition joints between ferritic and austenitic alloys. *J. Alloy. Comp.* **770**, 995–1003 (2019).
31. Ge, W., Lin, F. & Guo, C. in *Proc. 26th Annu. Int. Solid Freeform Fabrication Symp. — An Addit. Manuf. Conf*. (eds Bourell, D. L., Crawford, R.H., Seepersad, C. C., Beaman, J., J., Fish, S. & Marcus, H.) 10–12 (The University of Texas, Austin, 2015).
32. Wang, F., Mei, J., Jiang, H. & Wu, X. H. Production of functionally-graded samples using simultaneous powder and wire-feed. *Mater. Sci. Forum.* **539**, 3631–3636 (2007).
33. Hofmann, D. C. et al. Developing gradient metal alloys through radial deposition additive manufacturing. *Sci. Rep.* **4**, 5357 (2014).
34. Bobbio, L. D. et al. Additive manufacturing of a functionally graded material from Ti–6Al–4V to Invar: experimental characterization and thermodynamic calculations. *Acta Mater.* **127**, 133–142 (2017).
35. Gan, Z., Yu, G., He, X. & Li, S. Numerical simulation of thermal behavior and multicomponent mass transfer in direct laser deposition of Co-base alloy on steel. *Int. J. Heat Mass Transf.* **104**, 28–38 (2017).
36. Eliseeva, O. et al. Functionally graded materials through robotics-inspired path planning. *Mater. Des.* **182**, 107975 (2019).
37. Wang, Y. M. et al. Additively manufactured hierarchical stainless steels with high strength and ductility. *Nat. Mater.* **17**, 63 (2018).
38. Yin, Y., Sun, J., Guo, J., Kan, X. & Yang, D. Mechanism of high yield strength and yield ratio of 316 L stainless steel by additive manufacturing. *Mater. Sci. Eng. A* **744**, 773–777 (2019).
39. Liu, L. et al. Dislocation network in additive manufactured steel breaks strength–ductility trade-off. *Mater. Today* **21**, 354–361 (2018).
40. Sun, Z., Tan, X., Tor, S. B. & Chua, C. K. Simultaneously enhanced strength and ductility for 3D-printed stainless steel 316L by selective laser melting. *NPG Asia Mater.* **10**, 127 (2018).
41. Pham, M., Dovgyy, B. & Hooper, P. Twinning induced plasticity in austenitic stainless steel 316L made by additive manufacturing. *Mater. Sci. Eng. A* **704**, 102–111 (2017).
42. Wang, D. et al. Selective laser melting under the reactive atmosphere: a convenient and efficient approach to fabricate ultrahigh strength commercially pure titanium without sacrificing ductility. *Mater. Sci. Eng. A.* **762**, 138078 (2019).
43. Zhou, Y. et al. Selective laser melting enabled additive manufacturing of Ti–22Al–25Nb intermetallic: excellent combination of strength and ductility, and unique microstructural features associated. *Acta Mater.* **173**, 117–129 (2019).
44. Lin, J. et al. Enhanced strength and ductility in thin Ti–6Al–4V alloy components by alternating the thermal cycle strategy during plasma arc additive manufacturing. *Mater. Sci. Eng. A* **759**, 288–297 (2019).
45. De Formanoir, C. et al. Micromechanical behavior and thermal stability of a dual-phase $\alpha + \alpha'$ titanium alloy produced by additive manufacturing. *Acta Mater.* **162**, 149–162 (2019).
46. Sabban, R., Bahl, S., Chatterjee, K. & Suwas, S. Globularization using heat treatment in additively manufactured Ti–6Al–4V for high strength and toughness. *Acta Mater.* **162**, 239–254 (2019).
47. Azizi, H. et al. Additive manufacturing of a novel Ti–Al–V–Fe alloy using selective laser melting. *Addit. Manuf.* **21**, 529–535 (2018).
48. He, B. et al. Microstructural characteristic and mechanical property of Ti6Al4V alloy fabricated by selective laser melting. *Vacuum* **150**, 79–83 (2018).
49. AlMangour, B., Kim, Y.-K., Grzesiak, D. & Lee, K.-A. Novel TiB2-reinforced 316L stainless steel nano-composites with excellent room- and high-temperature yield strength developed by additive manufacturing. *Compos. Part. B Eng.* **156**, 51–63 (2019).
50. Dong, Z., Kang, H., Xie, Y., Chi, C. & Peng, X. Effect of powder oxygen content on microstructure and mechanical properties of a laser additively-manufactured 12CrNi2 alloy steel. *Mater. Lett.* **236**, 214–217 (2019).
51. Suryawanshi, J. et al. Simultaneous enhancements of strength and toughness in an Al–12Si alloy synthesized using selective laser melting. *Acta Mater.* **115**, 285–294 (2016).
52. Wang, Z., Palmer, T. A. & Beese, A. M. Effect of processing parameters on microstructure and tensile properties of austenitic stainless steel 304L made by directed energy deposition additive manufacturing. *Acta Mater.* **110**, 226–235 (2016).
53. Dadbakhsh, S., Mertens, R., Hao, L., Van Humbeeck, J. & Kruth, J. P. Selective laser melting to manufacture “in situ” metal matrix composites: a review. *Adv. Eng. Mater.* **21**, 1801244 (2019).
54. Wang, Y., Shi, J., Deng, X. & Lu, S. in *ASME 2016 International Mechanical Engineering Congress and Exposition* https://doi.org/10.1115/IMECE2016-67304 (American Society of Mechanical Engineers Digital Collection, 2016).
55. Gu, D. et al. Laser additive manufacturing of nano-TiC reinforced Ni-based nanocomposites with tailored microstructure and performance. *Compos. Part. B Eng.* **163**, 585–597 (2019).
56. Gu, D., Cao, S. & Lin, K. Laser metal deposition additive manufacturing of TiC reinforced Inconel 625 composites: influence of the additive TiC particle and its starting size. *J. Manuf. Sci. Eng.* **139**, 041014 (2017).
57. Zhang, B. et al. Comparison of carbon-based reinforcement on laser aided additive manufacturing Inconel 625 composites. *Appl. Surf. Sci.* **490**, 522–534 (2019).
58. Li, X. P. et al. Selective laser melting of nano-TiB2 decorated AlSi10Mg alloy with high fracture strength and ductility. *Acta Mater.* **129**, 183–193 (2017).
59. Zhou, W. et al. In situ formation of uniformly dispersed Al4C3 nanorods during additive manufacturing of graphene oxide/Al mixed powders. *Carbon*. **141**, 67–75 (2019).
60. Du, Z., Tan, M. J., Guo, J. F., Chua, C. K. & Lim, J. J. D. The effect of laser power and scanning speed on the density of selective laser melting fabricated Al–CNT composites. *DR-NTU* https://hdl.handle.net/10356/84568 (Research Publishing, 2016).
61. Mereddy, S. et al. Trace carbon addition to refine microstructure and enhance properties of additive-manufactured Ti–6Al–4V. *JOM* **70**, 1670–1676 (2018).
62. Yu, W., Sing, S., Chua, C., Kuo, C. & Tian, X. Particle-reinforced metal matrix nanocomposites fabricated by selective laser melting: a state of the art review. *Prog. Mater. Sci.* **104**, 330–379 (2019).
63. Wei, H. L., Knapp, G. L., Mukherjee, T. & DebRoy, T. Three-dimensional grain growth during multi-layer printing of a nickel-based alloy Inconel 718. *Addit. Manuf.* **25**, 448–459 (2019).
64. Jadhav, S. et al. Influence of selective laser melting process parameters on texture evolution in pure copper. *J. Mater. Process. Tech.* **270**, 47–58 (2019).
65. Andreau, O. et al. Texture control of 316L parts by modulation of the melt pool morphology in selective laser melting. *J. Mater. Process. Tech.* **264**, 21–31 (2019).
66. Martin, J. H. et al. 3D printing of high-strength aluminium alloys. *Nature* **549**, 365 (2017).
67. Wen, X. et al. Laser solid forming additive manufacturing TiB2 reinforced 2024Al composite: microstructure and mechanical properties. *Mater. Sci. Eng. A* **745**, 319–325 (2019).
68. Bermingham, M. J., StJohn, D. H., Krynen, J., Tedman-Jones, S. & Dargusch, M. S. Promoting the columnar to equiaxed transition and grain refinement of titanium alloys during additive manufacturing. *Acta Mater.* **168**, 261–274 (2019).
69. Li, J. et al. Microstructures and mechanical properties of laser additive manufactured Al–5Si–1Cu–Mg alloy with different layer thicknesses. *J. Alloy. Comp.* **789**, 15–24 (2019).
70. Helmer, H., Bauereiβ, A., Singer, R. & Körner, C. Grain structure evolution in Inconel 718 during selective electron beam melting. *Mater. Sci. Eng. A* **668**, 180–187 (2016).
71. Haines, M., Plotkowski, A., Frederick, C., Schwalbach, E. & Babu, S. S. A sensitivity analysis of the columnar-to-equiaxed transition for Ni-based superalloys in electron beam additive manufacturing. *Comp. Mater. Sci.* **155**, 340–349 (2018).
72. Raghavan, N. et al. Localized melt-scan strategy for site specific control of grain size and primary dendrite arm spacing in electron beam additive manufacturing. *Acta Mater.* **140**, 375–387 (2017).
73. Jia, Q. et al. Selective laser melting of a high strength AlMnSc alloy: alloy design and strengthening mechanisms. *Acta Mater.* **171**, 108–118 (2019).
74. Todaro, C. J. et al. Grain structure control during metal 3D printing by high-intensity ultrasound. *Nat. Commun.* **11**, 142 (2020).
75. Lee, H. W., Jung, K.-H., Hwang, S.-K., Kang, S.-H. & Kim, D.-K. Microstructure and mechanical anisotropy of CoCrW alloy processed by selective laser melting. *Mater. Sci. Eng. A* **749**, 65–73 (2019).
76. Bahl, S. et al. Non-equilibrium microstructure, crystallographic texture and morphological texture synergistically result in unusual mechanical properties of 3D printed 316L stainless steel. *Addit. Manuf.* **28**, 65–77 (2019).
77. Gordon, J., Hochhalter, J., Haden, C. & Harlow, D. G. Enhancement in fatigue performance of metastable austenitic stainless steel through directed energy deposition additive manufacturing. *Mater. Des.* **168**, 107630 (2019).
78. Tarasov, S. Y. et al. Microstructural evolution and chemical corrosion of electron beam wire-feed additively manufactured AISI 304 stainless steel. *J. Alloy. Comp.* **803**, 364–370 (2019).
79. Du, D. et al. Influence of build orientation on microstructure, mechanical and corrosion behavior of Inconel 718 processed by selective laser melting. *Mater. Sci. Eng. A* **760**, 469–480 (2019).
80. Wang, L. Y., Zhou, Z. J., Li, C. P., Chen, G. F. & Zhang, G. P. Comparative investigation of small punch creep resistance of Inconel 718 fabricated by selective laser melting. *Mater. Sci. Eng. A* **745**, 31–38 (2019).
81. Dinda, G., Dasgupta, A. & Mazumder, J. Texture control during laser deposition of nickel-based superalloy. *Scr. Mater.* **67**, 503–506 (2012).
82. Wei, H. L., Mazumder, J. & DebRoy, T. Evolution of solidification texture during additive manufacturing. *Sci. Rep.* **5**, 16446 (2015).
83. Carlton, H. D., Klein, K. D. & Elmer, J. W. Evolution of microstructure and mechanical properties of selective laser melted Ti–5Al–5V–5Mo–3Cr after heat treatments. *Sci. Technol. Weld. Join.* **24**, 465–473 (2019).
84. Thijs, L., Kempen, K., Kruth, J. P. & Van Humbeeck, J. Fine-structured aluminium products with controllable texture by selective laser melting of pre-alloyed AlSi10Mg powder. *Acta Mater.* **61**, 1809–1819 (2013).
85. Garibaldi, M., Ashcroft, I., Simonelli, M. & Hague, R. Metallurgy of high-silicon steel parts produced using selective laser melting. *Acta Mater.* **110**, 207–216 (2016).
86. Antonysamy, A. A., Meyer, J. & Prangnell, P. B. Effect of build geometry on the β-grain structure and texture in additive manufacture of Ti6Al4V by selective electron beam melting. *Mater. Charact.* **84**, 153–168 (2013).
87. Ocelík, V., Furár, I. & De Hosson, J. T. M. Microstructure and properties of laser clad coatings studied by orientation imaging microscopy. *Acta Mater.* **58**, 6763–6772 (2010).
88. Bhattacharya, S., Dinda, G. P., Dasgupta, A. K. & Mazumder, J. A comparative study of microstructure and mechanical behavior of CO_2 and diode laser deposited Cu–38Ni alloy. *J. Mater. Sci.* **49**, 2415–2429 (2014).
89. Dinda, G. P., Dasgupta, A. K. & Mazumder, J. Evolution of microstructure in laser deposited Al–11.28%Si alloy. *Surf. Coat. Tech.* **206**, 2152–2160 (2012).
90. Kontis, P. et al. Atomic-scale grain boundary engineering to overcome hot-cracking in additively-manufactured superalloys. *Acta Mater.* **177**, 209–221 (2019).
91. Dryburgh, P. et al. Spatially resolved acoustic spectroscopy for integrity assessment in wire–arc additive manufacturing. *Addit. Manuf.* **28**, 236–251 (2019).
92. Patel, R. et al. Imaging material texture of as-deposited selective laser melted parts using spatially resolved acoustic spectroscopy. *Appl. Sci.* **8**, 1991 (2018).
93. Everton, S. K., Hirsch, M., Stravroulakis, P., Leach, R. K. & Clare, A. T. Review of in-situ process monitoring and in-situ metrology for metal additive manufacturing. *Mater. Des.* **95**, 431–445 (2016).

94. Koepf, J. A., Gotterbarm, M. R., Markl, M. & Körner, C. 3D multi-layer grain structure simulation of powder bed fusion additive manufacturing. *Acta Mater.* **152**, 119–126 (2018).
95. Coeck, S., Bisht, M., Plas, J. & Verbist, F. Prediction of lack of fusion porosity in selective laser melting based on melt pool monitoring data. *Addit. Manuf.* **25**, 347–356 (2019).
96. Mukherjee, T., Zuback, J. S., Zhang, W. & DebRoy, T. Residual stresses and distortion in additively manufactured compositionally graded and dissimilar joints. *Comp. Mater. Sci.* **143**, 325–337 (2018).
97. Cunningham, R. et al. Keyhole threshold and morphology in laser melting revealed by ultrahigh-speed X-ray imaging. *Science* **363**, 849–852 (2019).
98. Martin, A. A. et al. Dynamics of pore formation during laser powder bed fusion additive manufacturing. *Nat. Commun.* **10**, 1987 (2019).
99. Ge, J. et al. Wire-arc additive manufacturing H13 part: 3D pore distribution, microstructural evolution, and mechanical performances. *J. Alloy. Comp.* **783**, 145–155 (2019).
100. Yu, W., Sing, S. L., Chua, C. K. & Tian, X. Influence of re-melting on surface roughness and porosity of AlSi10Mg parts fabricated by selective laser melting. *J. Alloy. Comp.* **792**, 574–581 (2019).
101. Leung, C. L. A. et al. The effect of powder oxidation on defect formation in laser additive manufacturing. *Acta Mater.* **166**, 294–305 (2019).
102. Tillmann, W. et al. Hot isostatic pressing of IN718 components manufactured by selective laser melting. *Addit. Manuf.* **13**, 93–102 (2017).
103. AlMangour, B., Grzesiak, D. & Yang, J.-M. Selective laser melting of TiB2/H13 steel nanocomposites: influence of hot isostatic pressing post-treatment. *J. Mater. Process. Technol.* **244**, 344–353 (2017).
104. Khomutov, M. et al. Effect of hot isostatic pressing on structure and properties of intermetallic NiAl–Cr–Mo alloy produced by selective laser melting. *Intermetallics* **120**, 106766 (2020).
105. Kou, S. A criterion for cracking during solidification. *Acta Mater.* **88**, 366–374 (2015).
106. Withers, P. J. & Bhadeshia, H. Residual stress. Part 2—nature and origins. *Mater. Sci. Technol.* **17**, 366–375 (2001).
107. Levkulich, N. C. et al. The effect of process parameters on residual stress evolution and distortion in the laser powder bed fusion of Ti–6Al–4V. *Addit. Manuf.* **28**, 475–484 (2019).
108. Onuike, B. & Bandyopadhyay, A. Additive manufacturing of Inconel 718–Ti6Al4V bimetallic structures. *Addit. Manuf.* **22**, 844–851 (2018).
109. Li, C., Liu, Z. Y., Fang, X. Y. & Guo, Y. B. Residual stress in metal additive manufacturing. *Procedia CIRP* **71**, 348–353 (2018).
110. Lu, X. et al. Residual stress and distortion of rectangular and S-shaped Ti–6Al–4V parts by directed energy deposition: modelling and experimental calibration. *Addit. Manuf.* **26**, 166–179 (2019).
111. Tyagi, P. et al. Reducing the roughness of internal surface of an additive manufacturing produced 316 steel component by chempolishing and electropolishing. *Addit. Manuf.* **25**, 32–38 (2019).
112. Bhaduri, D. et al. Evaluation of surface/interface quality, microstructure and mechanical properties of hybrid additive–subtractive aluminium parts. *CIRP Ann.* **68**, 237–240 (2019).
113. Yang, T. et al. The influence of process parameters on vertical surface roughness of the AlSi10Mg parts fabricated by selective laser melting. *J. Mater. Process. Technol.* **266**, 26–36 (2019).
114. Chen, Z., Wu, X., Tomus, D. & Davies, C. H. J. Surface roughness of selective laser melted Ti–6Al–4V alloy components. *Addit. Manuf.* **21**, 91–103 (2018).
115. Derekar, K. S. A review of wire arc additive manufacturing and advances in wire arc additive manufacturing of aluminium. *Mater. Sci. Technol.* **34**, 895–916 (2018).
116. Ali, U. et al. Identification and characterization of spatter particles and their effect on surface roughness, density and mechanical response of 17-4 PH stainless steel laser powder-bed fusion parts. *Mater. Sci. Eng. A* **756**, 98–107 (2019).
117. Cao, L. Numerical simulation of the impact of laying powder on selective laser melting single-pass formation. *Int. J. Heat Mass Transf.* **141**, 1036–1048 (2019).
118. Manvatkar, V., De, A. & DebRoy, T. Heat transfer and material flow during laser assisted multi-layer additive manufacturing. *J. Appl. Phys.* **116**, 124905 (2014).
119. Mukherjee, T., Wei, H. L., De, A. & DebRoy, T. Heat and fluid flow in additive manufacturing — Part I: modeling of powder bed fusion. *Comput. Mater. Sci.* **150**, 304–313 (2018).
120. Ou, W., Mukherjee, T., Knapp, G. L., Wei, Y. & DebRoy, T. Fusion zone geometries, cooling rates and solidification parameters during wire arc additive manufacturing. *Int. J. Heat Mass Transf.* **127**, 1084–1094 (2018).
121. Mukherjee, T., Wei, H. L., De, A. & DebRoy, T. Heat and fluid flow in additive manufacturing — Part II: powder bed fusion of stainless steel, and titanium, nickel and aluminum base alloys. *Comput. Mater. Sci.* **150**, 369–380 (2018).
122. Knapp, G. L. et al. Building blocks for a digital twin of additive manufacturing. *Acta Mater.* **135**, 390–399 (2017).
123. Mukherjee, T. & DebRoy, T. Printability of 316 stainless steel. *Sci. Technol. Weld. Join.* **24**, 412–419 (2019).
124. Mukherjee, T., Zuback, J. S., De, A. & DebRoy, T. Printability of alloys for additive manufacturing. *Sci. Rep.* **6**, 19717 (2016).
125. Tan, J. H. K., Sing, S. L. & Yeong, W. Y. Microstructure modelling for metallic additive manufacturing: a review. *Virtual Phys. Prototyp.* **15**, 87–105 (2020).
126. Bhadeshia, H., Svensson, L.-E. & Gretoft, B. A model for the development of microstructure in low-alloy steel (Fe–Mn–Si–C) weld deposits. *Acta Metall.* **33**, 1271–1283 (1985).
127. Li, X. & Tan, W. Numerical investigation of effects of nucleation mechanisms on grain structure in metal additive manufacturing. *Comput. Mater. Sci.* **153**, 159–169 (2018).
128. Nie, P., Ojo, O. A. & Li, Z. Numerical modeling of microstructure evolution during laser additive manufacturing of a nickel-based superalloy. *Acta Mater.* **77**, 85–95 (2014).
129. Yang, Y., Jamshidinia, M., Boulware, P. & Kelly, S. Prediction of microstructure, residual stress, and deformation in laser powder bed fusion process. *Comput. Mech.* **61**, 599–615 (2018).
130. Baykasoglu, C., Akyildiz, O., Candemir, D., Yang, Q. & To, A. C. Predicting microstructure evolution during directed energy deposition additive manufacturing of Ti–6Al–4V. *J. Manuf. Sci. Eng.* **140**, 051003 (2018).
131. Sui, S. et al. The influence of Laves phases on the room temperature tensile properties of Inconel 718 fabricated by powder feeding laser additive manufacturing. *Acta Mater.* **164**, 413–427 (2019).
132. Qin, R. & Bhadeshia, H. Phase field method. *Mater. Sci. Technol.* **26**, 803–811 (2010).
133. Zheng, W. et al. Phase field investigation of dendrite growth in the welding pool of aluminum alloy 2A14 under transient conditions. *Comput. Mater. Sci.* **82**, 525–530 (2014).
134. Keller, T. et al. Application of finite element, phase-field, and CALPHAD-based methods to additive manufacturing of Ni-based superalloys. *Acta Mater.* **139**, 244–253 (2017).
135. Shi, R. et al. Integrated simulation framework for additively manufactured Ti–6Al–4V: melt pool dynamics, microstructure, solid-state phase transformation, and microelastic response. *JOM* **71**, 3640–3655 (2019).
136. Lian, Y., Lin, S., Yan, W., Liu, W. K. & Wagner, G. J. A parallelized three-dimensional cellular automaton model for grain growth during additive manufacturing. *Comput. Mech.* **61**, 543–558 (2018).
137. Rodgers, T. M., Madison, J. D. & Tikare, V. Simulation of metal additive manufacturing microstructures using kinetic Monte Carlo. *Comput. Mater. Sci.* **135**, 78–89 (2017).
138. Mukherjee, T., Zhang, W. & DebRoy, T. An improved prediction of residual stresses and distortion in additive manufacturing. *Comput. Mater. Sci.* **126**, 360–372 (2017).
139. Mukherjee, T., Manvatkar, V., De, A. & DebRoy, T. Mitigation of thermal distortion during additive manufacturing. *Scr. Mater.* **127**, 79–83 (2017).
140. Wang, Z., Yan, W., Liu, W. K. & Liu, M. Powder-scale multi-physics modeling of multi-layer multi-track selective laser melting with sharp interface capturing method. *Comput. Mech.* **63**, 649–661 (2019).
141. Lee, Y. & Zhang, W. Modeling of heat transfer, fluid flow and solidification microstructure of nickel-base superalloy fabricated by laser powder bed fusion. *Addit. Manuf.* **12**, 178–188 (2016).
142. Tang, C., Tan, J. L. & Wong, C. H. A numerical investigation on the physical mechanisms of single track defects in selective laser melting. *Int. J. Heat Mass Transf.* **126**, 957–968 (2018).
143. Khairallah, S. A., Anderson, A. T., Rubenchik, A. & King, W. E. Laser powder-bed fusion additive manufacturing: physics of complex melt flow and formation mechanisms of pores, spatter, and denudation zones. *Acta Mater.* **108**, 36–45 (2016).
144. Knoll, H. et al. Combinatorial alloy design by laser additive manufacturing. *Steel Res. Int.* **88**, 1600416 (2017).
145. Schwendner, K. I., Banerjee, R., Collins, P. C., Brice, C. A. & Fraser, H. L. Direct laser deposition of alloys from elemental powder blends. *Scr. Mater.* **45**, 1123–1129 (2001).
146. Aversa, A. et al. New aluminum alloys specifically designed for laser powder bed fusion: a review. *Materials* **12**, 1007 (2019).
147. Mitchell, T. M. *Machine Learning* (McGraw-Hill, 1997).
148. LeCun, Y., Bengio, Y. & Hinton, G. Deep learning. *Nature* **521**, 436–444 (2015).
149. Jordan, M. I. & Mitchell, T. M. Machine learning: trends, perspectives, and prospects. *Science* **349**, 255–260 (2015).
150. Zhang, B., Jaiswal, P., Rai, R., Guerrier, P. & Baggs, G. Convolutional neural network-based inspection of metal additive manufacturing parts. *Rapid Prototyp. J.* **25**, 530–540 (2019).
151. Aoyagi, K., Wang, H., Sudo, H. & Chiba, A. Simple method to construct process maps for additive manufacturing using a support vector machine. *Addit. Manuf.* **27**, 353–362 (2019).
152. Wang, Y., Blache, R., Zheng, P. & Xu, X. A knowledge management system to support design for additive manufacturing using Bayesian networks. *J. Mech. Des.* **140**, 051701 (2018).
153. Wu, D., Wei, Y. & Terpenny, J. Predictive modelling of surface roughness in fused deposition modelling using data fusion. *Int. J. Prod. Res.* **57**, 3992–4006 (2019).
154. Zhao, Z., Guo, Y., Bai, L., Wang, K. & Han, J. Quality monitoring in wire-arc additive manufacturing based on cooperative awareness of spectrum and vision. *Optik* **181**, 351–360 (2019).
155. Du, Y., Mukherjee, T. & DebRoy, T. Conditions for void formation in friction stir welding from machine learning. *NPJ Comput. Mater.* **5**, 68 (2019).
156. Xiong, J., Zhang, G., Hu, J. & Wu, L. Bead geometry prediction for robotic GMAW-based rapid manufacturing through a neural network and a second-order regression analysis. *J. Intell. Manuf.* **25**, 157–163 (2014).
157. Ding, D. et al. Towards an automated robotic arc-welding-based additive manufacturing system from CAD to finished part. *Comput. Aid. Des.* **73**, 66–75 (2016).
158. Kappes, B., Moorthy, S., Drake, D., Geerlings, H. & Stebner, A. in *Proc. 9th Int. Symp. on Superalloy 718 & Derivatives: Energy, Aerospace, and Industrial Applications* (eds Ott, E., Liu, X., Andersson, J., Bi, Z., Bockenstedt, K., Dempster, I., Groh, J., Heck, K., Jablonski, P., Kaplan, M., Nagahama, D. & Sudbrack, C.) 595–610 (Springer, 2018).
159. Zhang, W., Mehta, A., Desai, P. S. & Higgs, C. in *Int. Solid Freeform Fabrication Symp*. (eds Bourell, D. L., Crawford, R. H., Seepersad, C. C., Beaman, J. J. & Fish, S.) 1235–1249 (The University of Texas, Austin, 2017).
160. Rosa, B., Mognol, P. & Hascoët, J.-Y. Modelling and optimization of laser polishing of additive laser manufacturing surfaces. *Rapid Prototyp. J.* **22**, 956–964 (2016).
161. Imani, F., Chen, R., Diewald, E., Reutzel, E. & Yang, H. Deep learning of variant geometry in layerwise imaging profiles for additive manufacturing quality control. *J. Manuf. Sci. Eng.* **141**, 111001 (2019).
162. DeCost, B. L., Jain, H., Rollett, A. D. & Holm, E. A. Computer vision and machine learning for autonomous characterization of AM powder feedstocks. *JOM* **69**, 456–465 (2017).
163. Amini, M. & Chang, S. I. MLCPM: a process monitoring framework for 3D metal printing in industrial scale. *Comput. Ind. Eng.* **124**, 322–330 (2018).
164. Mazumder, J. Design for metallic additive manufacturing machine with capability for "Certify as You Build". *Procedia CIRP* **36**, 187–192 (2015).
165. Wu, Q., Mukherjee, T., Liu, C., Lu, J. & DebRoy, T. Residual stresses and distortion in the patterned printing of titanium and nickel alloys. *Addit. Manuf.* **29**, 100808 (2019).
166. Yuan, B. et al. Machine-learning-based monitoring of laser powder bed fusion. *Adv. Mater. Technol.* **3**, 1800136 (2018).
167. Caiazzo, F. & Caggiano, A. Laser direct metal deposition of 2024 Al alloy: trace geometry prediction via machine learning. *Materials* **11**, 444 (2018).

168. Kamath, C. Data mining and statistical inference in selective laser melting. *Int. J. Adv. Manuf. Technol.* **86**, 1659–1677 (2016).
169. Zhu, Z., Anwer, N., Huang, Q. & Mathieu, L. Machine learning in tolerancing for additive manufacturing. *CIRP Ann.* **67**, 157–160 (2018).
170. Wan, H., Chen, G., Li, C., Qi, X. & Zhang, G. Data-driven evaluation of fatigue performance of additive manufactured parts using miniature specimens. *J. Mater. Sci. Technol.* **35**, 1137–1146 (2019).
171. Popova, E. et al. Process-structure linkages using a data science approach: application to simulated additive manufacturing data. *Integr. Mater. Manuf. Innov.* **6**, 54–68 (2017).
172. Collins, P. C. et al. Progress toward an integration of process–structure–property–performance models for "three-dimensional (3-D) printing" of titanium alloys. *JOM* **66**, 1299–1309 (2014).
173. Khanzadeh, M., Chowdhury, S., Marufuzzaman, M., Tschopp, M. A. & Bian, L. Porosity prediction: supervised-learning of thermal history for direct laser deposition. *J. Manuf. Syst.* **47**, 69–82 (2018).
174. Scime, L. & Beuth, J. A multi-scale convolutional neural network for autonomous anomaly detection and classification in a laser powder bed fusion additive manufacturing process. *Addit. Manuf.* **24**, 273–286 (2018).
175. Scime, L. & Beuth, J. Anomaly detection and classification in a laser powder bed additive manufacturing process using a trained computer vision algorithm. *Addit. Manuf.* **19**, 114–126 (2018).
176. Bharadwaj, R. Artificial intelligence applications in additive manufacturing (3D printing). *Emerj — Artificial Intelligence Research and Insight* https://emerj.com/ai-sector-overviews/artificial-intelligence-applications-additive-manufacturing-3d-printing/ (2019).
177. Ali, A. B. Deep learning for advanced additive manufacturing. *Medium* https://medium.com/@amynebenali/deep-learning-for-advanced-additive-manufacturing-65157e7a1b06 (2018).
178. Du, Y., Mukherjee, T., Mitra, P. & DebRoy, T. Machine learning based hierarchy of causative variables for tool failure in friction stir welding. *Acta Mater.* **192**, 67–77 (2020).
179. Tofail, S. A. et al. Additive manufacturing: scientific and technological challenges, market uptake and opportunities. *Mater. Today* **21**, 22–37 (2018).
180. Johnson, L. et al. Assessing printability maps in additive manufacturing of metal alloys. *Acta Mater.* **176**, 199–210 (2019).
181. Huang, D. J. & Li, H. in *Proc. 3rd Int. Conf. Progress Addit. Manuf*. (eds Chua, C. K, Yeong, W. Y., Tan, M. J., Liu, E. & Tor, S. B.) (Pro-AM, 2018).
182. Li, B.-h, Hou, B.-c, Yu, W.-t, Lu, X.-b & Yang, C.-w. Applications of artificial intelligence in intelligent manufacturing: a review. *Front. Inf. Technol. Electron. Eng.* **18**, 86–96 (2017).
183. Qi, Q. & Tao, F. Digital twin and big data towards smart manufacturing and industry 4.0: 360 degree comparison. *IEEE Access.* **6**, 3585–3593 (2018).
184. Wohlers, T., Caffrey, T., Campbell, R. I., Diegel, O. & Kowen, J. *Wohlers Report 2018: 3D Printing and Additive Manufacturing State of the Industry; Annual Worldwide Progress Report* (Wohlers Associates, 2018).
185. Mukherjee, T. & DebRoy, T. Mitigation of lack of fusion defects in powder bed fusion additive manufacturing. *J. Manuf. Process.* **36**, 442–449 (2018).
186. 3DscienceValley. Digital Alloys' guide to metal additive manufacturing — Part 13, Joule Printing™ vs wire DED. *Digital Alloys* https://www.digitalalloys.com/blog/joule-printing-vs-wire-ded (2019).
187. Donoghue, J. et al. The effectiveness of combining rolling deformation with wire–arc additive manufacture on β-grain refinement and texture modification in Ti–6Al–4V. *Mater. Charact.* **114**, 103–114 (2016).
188. Majeed, M., Khan, H. & Rasheed, I. Finite element analysis of melt pool thermal characteristics with passing laser in SLM process. *Optik* **194**, 163068 (2019).
189. Khan, K. & De, A. Modelling of selective laser melting process with adaptive remeshing. *Sci. Technol. Weld. Join.* **24**, 391–400 (2019).
190. Huang, Y. et al. Rapid prediction of real-time thermal characteristics, solidification parameters and microstructure in laser directed energy deposition (powder-fed additive manufacturing). *J. Mater. Process. Technol.* **274**, 116286 (2019).
191. Bai, X. et al. Numerical analysis of heat transfer and fluid flow in multilayer deposition of PAW-based wire and arc additive manufacturing. *Int. J. Heat Mass Transf.* **124**, 504–516 (2018).
192. He, X. & Mazumder, J. Transport phenomena during direct metal deposition. *J. Appl. Phys.* **101**, 053113 (2007).
193. Klassen, A., Scharowsky, T. & Körner, C. Evaporation model for beam based additive manufacturing using free surface lattice Boltzmann methods. *J. Phys. D. Appl. Phys.* **47**, 275303 (2014).
194. Rausch, A. M., Markl, M. & Körner, C. Predictive simulation of process windows for powder bed fusion additive manufacturing: influence of the powder size distribution. *Comput. Math. Appl.* **78**, 2351–2359 (2019).
195. Lindwall, G. et al. Simulation of TTT curves for additively manufactured Inconel 625. *Metall. Mater. Trans. A* **50**, 457–467 (2019).
196. Rai, A., Markl, M. & Körner, C. A coupled cellular automaton–lattice Boltzmann model for grain structure simulation during additive manufacturing. *Comput. Mater. Sci.* **124**, 37–48 (2016).
197. Zhang, Z. et al. Numerical methods for microstructural evolutions in laser additive manufacturing. *Comput. Math. Appl.* **78**, 2296–2307 (2019).
198. Wang, Y., Shi, J. & Liu, Y. Competitive grain growth and dendrite morphology evolution in selective laser melting of Inconel 718 superalloy. *J. Cryst. Growth* **521**, 15–29 (2019).
199. Kumara, C. et al. Predicting the microstructural evolution of electron beam melting of alloy 718 with phase-field modeling. *Metall. Mater. Trans. A* **50**, 2527–2537 (2019).
200. Schänzel, M., Shakirov, D., Ilin, A. & Ploshikhin, V. Coupled thermo-mechanical process simulation method for selective laser melting considering phase transformation steels. *Comput. Math. Appl.* **78**, 2230–2246 (2019).
201. Denlinger, E. R., Gouge, M., Irwin, J. & Michaleris, P. Thermomechanical model development and in situ experimental validation of the laser powder-bed fusion process. *Addit. Manuf.* **16**, 73–80 (2017).
202. Caggiano, A. et al. Machine learning-based image processing for on-line defect recognition in additive manufacturing. *CIRP Ann.* **68**, 451–454 (2019).
203. Chowdhury, S. & Anand, S. in *ASME 2016 11th Int. Manuf. Sci. Eng. Conf*. https://doi.org/10.1115/MSEC2016-8784 (American Society of Mechanical Engineers Digital Collection, 2016).
204. Dastjerdi, A. A., Movahhedy, M. R. & Akbari, J. Optimization of process parameters for reducing warpage in selected laser sintering of polymer parts. *Addit. Manuf.* **18**, 285–294 (2017).
205. Shevchik, S. A., Kenel, C., Leinenbach, C. & Wasmer, K. Acoustic emission for in situ quality monitoring in additive manufacturing using spectral convolutional neural networks. *Addit. Manuf.* **21**, 598–604 (2018).
206. Shevchik, S. A., Masinelli, G. G., Kenel, C., Leinenbach, C. & Wasmer, K. Deep learning for in situ and real-time quality monitoring in additive manufacturing using acoustic emission. *IEEE Trans. Industr. Inform.* **15**, 5194–5203 (2019).
207. Wei, Q., Akrotirianakis, I., Dasgupta, A. & Chakraborty, A. Learn to learn: application to topology optimization. *Smart Sust. Manuf. Syst.* **2**, 250–260 (2018).
208. Barrios, J. M. & Romero, P. E. Decision tree methods for predicting surface roughness in fused deposition modeling parts. *Materials* **12**, 2574 (2019).
209. Tootooni, M. S. et al. Classifying the dimensional variation in additive manufactured parts from laser-scanned three-dimensional point cloud data using machine learning approaches. *J. Manuf. Sci. Eng.* **139**, 091005 (2017).
210. He, H., Yang, Y. & Pan, Y. Machine learning for continuous liquid interface production: printing speed modelling. *J. Manuf. Syst.* **50**, 236–246 (2019).
211. Gordon, E. R. et al. in *Sustainable Design and Manufacturing 2016* (eds Setchi, R., Howlett, R. J., Liu Y. & Theobald, P.) 423–434 (Springer International, 2016).
212. Gobert, C., Reutzel, E. W., Petrich, J., Nassar, A. R. & Phoha, S. Application of supervised machine learning for defect detection during metallic powder bed fusion additive manufacturing using high resolution imaging. *Addit. Manuf.* **21**, 517–528 (2018).
213. Song, L., Huang, W., Han, X. & Mazumder, J. Real-time composition monitoring using support vector regression of laser-induced plasma for laser additive manufacturing. *IEEE Trans. Ind. Electron.* **64**, 633–642 (2016).
214. Zhang, J., Wang, P. & Gao, R. X. Deep learning-based tensile strength prediction in fused deposition modeling. *Comput. Ind.* **107**, 11–21 (2019).
215. Chen, Z., Zong, X., Shi, J. & Zhang, X. Online monitoring based on temperature field features and prediction model for selective laser sintering process. *Appl. Sci.* **8**, 2383 (2018).
216. Aminzadeh, M. & Kurfess, T. R. Online quality inspection using Bayesian classification in powder-bed additive manufacturing from high-resolution visual camera images. *J. Intell. Manuf.* **30**, 2505–2523 (2019).
217. Bacha, A., Sabry, A. H. & Benhra, J. Fault diagnosis in the field of additive manufacturing (3D printing) using Bayesian networks. *Int. J. Online Eng*. **15** (2019).
218. Li, J., Jin, R. & Hang, Z. Y. Integration of physically-based and data-driven approaches for thermal field prediction in additive manufacturing. *Mater. Des.* **139**, 473–485 (2018).
219. Tapia, G., Elwany, A. & Sang, H. Prediction of porosity in metal-based additive manufacturing using spatial Gaussian process models. *Addit. Manuf.* **12**, 282–290 (2016).
220. Aboutaleb, A. M. et al. Accelerated process optimization for laser-based additive manufacturing by leveraging similar prior studies. *IISE Trans.* **49**, 31–44 (2017).
221. Tapia, G., Khairallah, S., Matthews, M., King, W. E. & Elwany, A. Gaussian process-based surrogate modeling framework for process planning in laser powder-bed fusion additive manufacturing of 316L stainless steel. *Int. J. Adv. Manuf. Technol.* **94**, 3591–3603 (2018).
222. Martínez, J., Song, H., Dumas, J. & Lefebvre, S. Orthotropic *k*-nearest foams for additive manufacturing. *ACM Trans. Graph.* **36**, 121 (2017).
223. Mutiargo, B., Garbout, A. & Malcolm, A. A. in *International Forum on Medical Imaging in Asia 2019* 110500L (International Society for Optics and Photonics, 2019).
224. Wu, M., Phoha, V. V., Moon, Y. B. & Belman, A. K. in *ASME 2016 Int. Mech. Eng. Congress Exposition* https://doi.org/10.1115/IMECE201667641 (American Society of Mechanical Engineers Digital Collection, 2016).
225. Qin, J., Liu, Y. & Grosvenor, R. A framework of energy consumption modelling for additive manufacturing using Internet of Things. *Procedia CIRP* **63**, 307–312 (2017).
226. Alwoimi, B. M. *Development of a Framework for Design for Additive Manufacturing* (North Carolina A&T State University, 2018).
227. Chou, R., Ghosh, A., Chou, S., Paliwal, M. & Brochu, M. Microstructure and mechanical properties of Al10SiMg fabricated by pulsed laser powder bed fusion. *Mater. Sci. Eng. A* **689**, 53–62 (2017).
228. Baturynska, I., Semeniuta, O. & Wang, K. in *Advanced Manufacturing and Automation VIII. IWAMA 2018. Lecture Notes in Electrical Engineering* Vol 484 (eds Wang, K., Wang, Y., Strandhagen, J. & Yu, T.) 245–252 (Springer, 2019).
229. Paul, A. et al. A real-time iterative machine learning approach for temperature profile prediction in additive manufacturing processes in *2019 IEEE International Conference on Data Scienceand Advanced Analytics (DSAA)* (eds, Singh, L., De Veaux, R., Karypis, G., Bonchi,F. & Hill, J.) 541–550 (IEEE, Piscataway, 2019).
230. DeCost, B. L. & Holm, E. A. Characterizing powder materials using keypoint-based computer vision methods. *Comput. Mater. Sci.* **126**, 438–445 (2017).
231. Mitchell, J. A. *An Approach to Upscaling SPPARKS Generated Synthetic Microstructures of Additively Manufactured Metals* (Sandia National Lab., 2019).
232. Wang, Y., Lin, Y., Zhong, R. Y. & Xu, X. IoT-enabled cloud-based additive manufacturing platform to support rapid product development. *Int. J. Prod. Res.* **57**, 3975–3991 (2019).
233. Koeppe, A., Padilla, C. A. H., Voshage, M., Schleifenbaum, J. H. & Markert, B. Efficient numerical modeling of 3D-printed lattice-cell structures using neural networks. *Manuf. Lett.* **15**, 147–150 (2018).
234. Kunkel, M. H., Gebhardt, A., Mpofu, K. & Kallweit, S. Quality assurance in metal powder bed fusion via deep-learning-based image classification. *Rapid Prototyp. J.* (2019).
235. Francis, J. & Bian, L. Deep learning for distortion prediction in laser-based additive manufacturing using big data. *Manuf. Lett.* **20**, 10–14 (2019).
236. Mozaffar, M. et al. Data-driven prediction of the high-dimensional thermal history in directed energy deposition processes via recurrent neural networks. *Manuf. Lett.* **18**, 35–39 (2018).

237. Gonzalez-Val, C., Pallas, A., Panadeiro, V. & Rodriguez, A. A convolutional approach to quality monitoring for laser manufacturing. *J. Intell. Manuf.* **31**, 789–795 (2020).
238. Petrich, J., Gobert, C., Phoha, S., Nassar, A. R. & Reutzel, E. W. in *Proc. 27th Int. Solid Freeform Fabrication Symp*. (eds Bourell, D. L., Crawford, R. H., Seepersad, C. C., Beaman, J. J. & Fish, S.) 1660–1674 (The University of Texas, Austin, 2017).
239. Murphy, C., Meisel, N., Simpson, T. & McComb, C. in *Solid Freeform Fabrication 2018: Proc. 29th Annu. Int. Solid Freeform Fabrication Symp. — An Addit. Manuf. Conf*. (eds Bourell, D. L, Beaman, J. J., Crawford, R. H., Fish, S. & Seepersad, C., C.) 1363–1381 (The University of Texas, Austin, 2018).
240. Lu, X. et al. Open-source wire and arc additive manufacturing system: formability, microstructures, and mechanical properties. *Int. J. Adv. Manuf. Technol.* **93**, 2145–2154 (2017).
241. Gong, X. & Chou, K. Phase-field modeling of microstructure evolution in electron beam additive manufacturing. *JOM* **67**, 1176–1182 (2015).
242. Tan, J. L., Tang, C. & Wong, C. H. A computational study on porosity evolution in parts produced by selective laser melting. *Metall. Mater. Trans. A* **49**, 3663–3673 (2018).

Author contributions

All authors contributed in researching previous works, discussions of the contents of the manuscript, writing portions of the text and reviewing and editing the manuscript.

Competing Interests

The authors declare no competing interests.

Publisher's note

Springer Nature remains neutral with regard to jurisdictional claims in published maps and institutional affiliations.